

Review

# A Review of Blast Loading in the Urban Environment

Adam Ratcliff <sup>1,\*</sup>, Sam Rigby <sup>1,\*</sup> , Sam Clarke <sup>1</sup>  and Stephen Fay <sup>2</sup><sup>1</sup> Department of Civil and Structural Engineering, University of Sheffield, Sheffield S1 3JD, UK<sup>2</sup> Atomic Weapons Establishment, Damage Assessment, AWE Aldermaston, Reading RG7 4PR, UK

\* Correspondence: aratcliff1@sheffield.ac.uk (A.R.); sam.rigby@sheffield.ac.uk (S.R.)

**Abstract:** Urban blasts have become a significant concern in recent years. Whilst free-field blasts are well understood, the introduction of an urban setting (or any complex geometry) gives rise to multiple blast wave interactions and unique flow complexities, significantly increasing the difficulty of loading predictions. This review identifies commonly agreed-upon concepts or behaviours that are utilised to describe urban shock wave propagation, such as channelling and shielding, in conjunction with exploring urban characterisation metrics that aim to predict the effects on global blast loading for an urban blast. Likewise, discrepancies and contradictions are highlighted to promote key areas that require further work and clarification. Multiple numerical modelling programmes are acknowledged to showcase their ability to act as a means of validation and a preliminary testing tool. The findings contained within this review aim to inform future research decisions and topics better.

**Keywords:** numerical modelling; urban blasts; shock wave propagation; peak overpressure; scaled impulse

## 1. Introduction

The urban population density has consistently trended upward since records began and is predicted to continue doing so. Roughly 55% of the world's population was said to reside within urban areas in 2018; this figure is estimated to reach 68% in 2050 [1]. Additionally, explosions in urban settings are undoubtedly becoming more common. Terrorist attacks frequently target densely populated areas in order to generate media attention and cause fear. Improvised explosive devices (IEDs) are often used to target particular buildings or local areas with the specific intention of causing structural collapse and maximising the loss of life [2], as was the case of the 1995 Oklahoma bombing [3]. Accidental industrial explosions have the capacity to cause city-scale damage, as was seen in the aftermath of the 2020 Beirut explosion [4,5]. The war in Ukraine has further highlighted the need to understand blast events in urban environments, and this area also presents a significant challenge to military forces who require rapid numerical tools to assess combat scenarios in order to limit collateral damage and increase safety for friendly forces [6].

This dual increase in urbanisation and the magnitude and severity of explosions in urban areas has shifted blast protection engineering more towards the remit of the general structural engineer [7]. It is the aim of blast resilient design to provide protection strategies that are “*intelligent, thoughtful and holistic in approach, not blind and expensive hardening*” [8]. Accordingly, a detailed and comprehensive understanding of the blast load a structure or structural component may be subjected to is a crucial first step in facilitating a more focused and effective approach to blast protection engineering.

The prediction of blast loading in cityscapes is highly complex. When a blast wave propagates in a crowded setting, the magnitude and form of the resulting blast load differ substantially from those of a free-air blast, largely due to the confining effect of nearby structures [9]. Furthermore, the coalescence of multiple shock fronts that have reflected off or diffracted around obstacles is a highly non-linear physical process [10], and it has been



**Citation:** Ratcliff, A.; Rigby, S.; Clarke, S.; Fay, S. A Review of Blast Loading in the Urban Environment. *Appl. Sci.* **2023**, *13*, 5349. <https://doi.org/10.3390/app13095349>

Academic Editor: Ricardo Castedo

Received: 21 March 2023

Revised: 17 April 2023

Accepted: 21 April 2023

Published: 25 April 2023



**Copyright:** © 2023 by the authors. Licensee MDPI, Basel, Switzerland. This article is an open access article distributed under the terms and conditions of the Creative Commons Attribution (CC BY) license (<https://creativecommons.org/licenses/by/4.0/>).

shown that an accurate representation of the blast waveform is critically important when conducting quantitative risk assessments [11].

This literature review summarises the current state of the art regarding blast theory and identifies potential discrepancies between research papers to highlight topics for further investigation. Computational-based approaches are also reviewed to acknowledge their advantages and limitations for supplementing experimental work, and the review ends by exploring experimental methods and instrumentation to inform the methodology of future experimental work better. Whilst significant recent advancements have been made in each of these respective areas, it is hoped that this literature review will outline the common challenges still faced by the research community and discuss emerging solutions to them.

## 2. Current Knowledge

### 2.1. Basic Theory

The detonation of an explosive mass causes a shock front to propagate outwards through a substance. A shock wave can be considered as a near-instantaneous change in pressure, density, and internal energy that travels through a medium faster than the medium's speed of sound—approximately 343 m/s in air at ambient conditions. The resultant pressure increase above atmospheric pressure from the shock wave is defined as the peak overpressure, denoted as  $p_{so,max}$  for incident shock waves and  $p_{r,max}$  for reflected shock waves. The parameter  $t_a$  corresponds to the time of arrival (the duration it takes a shock wave to travel a given stand-off distance), and  $t_d$  represents the positive phase duration (i.e., the duration over which above ambient pressures are acting). The impulse values,  $i_{so}$  and  $i_r$ , are equal to the integral of their respective pressure curves with respect to time,  $t_d$ . The negative phase has a similar set of respective parameters, as described by Rigby et al. [12], detailed in Figure 1 as an ideal far-field blast wave.

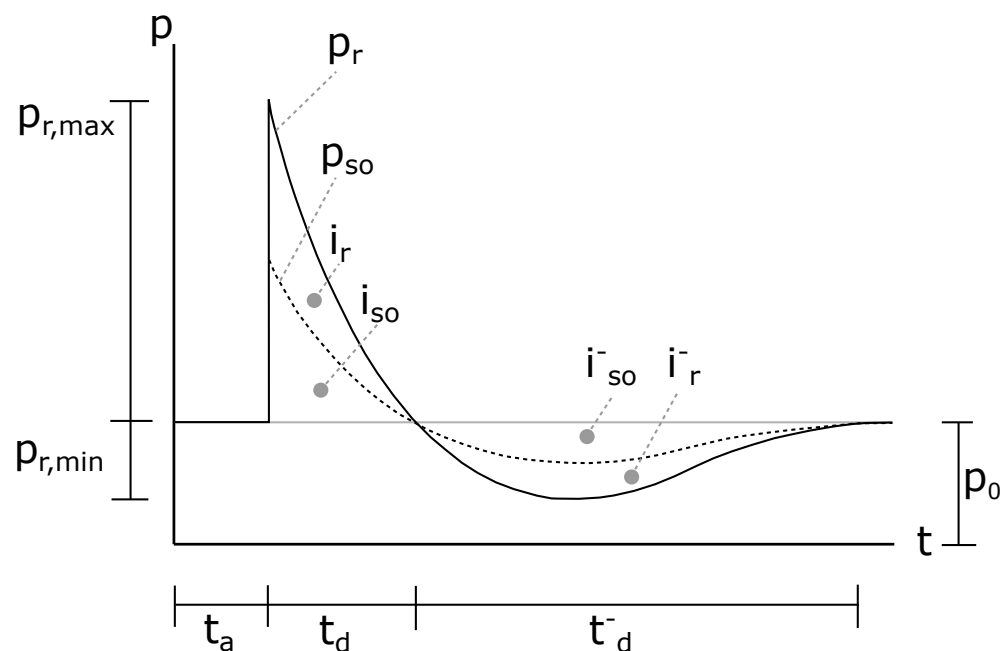


**Figure 1.** Pressure vs. time history curve that represents an ideal far-field blast wave, adapted from Rigby et al. [13].

Blast wave scaling is commonly used to compare geometrically similar explosive masses. Two geometrically similar shock waves will be produced upon the detonation of two geometrically similar explosive masses. The same scaled blast wave parameters will result from the two separate blasts, provided the scaled distances and control variables are identical [14]. The established scaling laws constitute cube-root scaling and were independently proposed by Hopkinson [15] and Craz [16], and hence the term “Hopkinson–Craz” scaling is often used.

Scaled distance,  $Z$ , can be calculated via Equation (1). These scaling laws allow direct comparisons between explosive events at any reasonable scale, provided the differences in the explosive compounds are accounted for (e.g., shape effects [17–20], secondary combustion [21], heat of detonation and/or reaction rates [22–25], etc.). However, some have previously suggested a practical limit to the minimum reasonable scale for gathering experimental data [26]. Johnson et al. [27] analysed the effectiveness of Hopkinson–Cranz scaling within tunnel environment-based blast tests. The difference between the peak overpressures between full-scale and small-scale tests was 3%, reinforcing the validity of the Hopkinson–Cranz scaling method.

$$Z = R/W^{1/3} \quad (1)$$

- $Z$  is the scaled distance ( $\text{m}/\text{kg}^{1/3}$ ).
- $R$  is the stand-off distance (m).
- $W$  is the explosive mass (kg, typically as an equivalent mass of TNT).

Trinitrotoluene (TNT) equivalency is a widely agreed-upon concept within the field of blast engineering [28], where TNT equivalence is defined as the mass of TNT required to produce the same blast parameter(s) of a unit mass of the explosive in question, at the same stand-off distance. This enables the comparison and prediction of blast wave parameters caused by the detonation of fundamentally different explosive compounds. Additionally, TNT is the explosive compound utilised in commonly used empirical formulae and computational calculators such as ConWep [29], Blast-X [30], EMBlast [31], etc. Therefore, TNT equivalency is required to analyse blast parameters using these approaches. The TNT equivalence factor for a given explosive compound can be calculated as seen in Equation (2).

$$TNT_{EQ} = W_{TNT}/W_{EC} \quad (2)$$

- $TNT_{EQ}$  is the TNT equivalence factor.
- $W_{TNT}$  is the mass of TNT that would create an “equivalent energy” blast compared to a mass of an explosive compound (kg).
- $W_{EC}$  is the mass of the explosive compound under investigation (kg).

Generally, these approaches are accepted for use within simple geometric scenarios, such as unimpeded air blasts, to predict blast wave parameters. However, in geometrically complex situations, the accuracy of these empirical methods is seen to diminish; thus, they are no longer deemed appropriate for accurate analyses. Smith and Rose [32] stated that “*simple tools are often inappropriate and the development of empirical rules for more complex geometries may not be reliable*”. Furthermore, Johnson et al. [27] stated that “*the ability to predict blast wave behaviour in confined environments would introduce a new avenue to inform blast resistant design for industrial processes*”.

## 2.2. Blasts Around Obstacles

Gautier et al. [33] analysed the interaction between a shock wave and a single obstacle through small-scale experimental work. The shock wave is generated via the detonation of a gaseous charge contained within a soap bubble (discussed further in Section 4.3.1). Two types of obstacles were tested, a cylinder and a parallelepiped. Each configuration was tested twice, once with the pressure sensors present and the other without. This was to avoid visual disturbances from the presence of the pressure sensors. Two cameras and an arrangement of mirrors permitted a front view and a plan view of the obstacles to be filmed. The visual and overpressure data were then superimposed in post-processing. It is stated that superimposing “*was possible only thanks to the good repeatability of the tests*”. The imaging setup used in the aforementioned work is discussed further in Section 4.1.3.

The findings highlight the potential benefits of multiple cameras, pitched perpendicularly to each other, to expose three-dimensional effects that cannot be detected using a

single camera or overpressure data alone. Regarding shock wave interaction with a finite object or an array of simple obstacles, it appears necessary to focus on imaging to ensure three-dimensional effects are detected [34].

Gautier et al. [35] also analysed the interaction between a blast wave and a wall of finite length. The thickness and height of the wall remained unchanged throughout at 18 mm and 82 mm, respectively. This ensured that the behavioural differences observed could be largely due to the length of the wall. Pressure sensors were placed on the same and opposite sides of the wall (relative to the charge centre) to allow for a free-field comparison.

Multiple wave behaviours were imaged clearly, allowing for a qualitative explanation of why the overpressure data varied from free-field propagation. The so-called “bypass” wave resulted from the incident wave that diffracted over the top side of the blast wall, and the trajectory of this wave remained similar for all configurations as the wall height was kept constant. The lateral waves consisted of two shocks that travelled along the length of the wall and diffracted around the lateral faces. They appeared to be slightly offset in the imaging; however, this resulted from a parallax from the imaging technique used (see Section 4.1.3), and they are, in fact, symmetrical. The trajectory of the lateral waves varied with each test as the wall length was altered.

For larger-length walls, the reduction in peak overpressure occurs in the immediate central area downstream of the wall, extending out to a distance similar to the height of the wall. This distance is seen to extend up to twice the height of the wall in other studies, [36]. Here, the wall sufficiently delayed the lateral waves so they do not interact with the bypass wave or its reflection near the wall. Further downstream for the medium-length walls, the maximum overpressure increased up to 40% compared to free-field propagation. This was attributed to the coalescence of the lateral and bypass waves. This is an important finding, as protecting a “close proximity” area to the wall may worsen loading at another area further downstream of the blast. It is hypothesised that only an infinite wall (or one of a conservatively substantial length) can guarantee overpressure mitigation. This also indicates that the assumption of free-field propagation in the presence of even a single and simple obstacle can be inaccurate.

### 2.3. Channelling and Shielding

Smith et al. [37] conducted experimental and numerical modelling to study the effects of areal density (defined as the percentage of the footprint area that consists of obstacles) and street layout on blast wave parameters. A singular wall was used as the point of interest for measuring pressure data, and the experimental work was shown to have good test-to-test repeatability. The computational software Air3D [38] was used to carry out the simulations, whereby a direct comparison was made to the experimental results for a particular setup. A good correlation was observed between the experimental and simulated results; thus, it was deemed suitable to continue the study via numerical methods only.

Two particular behaviours captured in this study were channelling and shielding. A control scenario was initially undertaken where a blast was simulated without any objects present. The distance variable relates to the distance along a 4 m wall perpendicular to the shock propagation (not the stand-off distance); hence, the middle of the wall has the shortest stand-off distance to the blast. The maximum peak overpressure was approximately 225 kPa in the control scenario.

The initial test scenarios had the same areal density, the critical difference being that the centre of the wall was shielded in one layout and was directly “down the street” in the other. These layouts were specifically chosen in an attempt to maximise both shielding and channelling behaviours, respectively. The layouts are illustrated in Figure 2. In the shielding-type layout, the central peak overpressure was 195 kPa, a 13.3% reduction compared to a no-obstacle scenario. In the channelling-type layout, a central peak overpressure of 305 kPa was recorded, a 35.5% increase compared to a no-obstacle scenario. Considering this pressure data, it is clear that obstacles between a blast and its target can significantly affect peak overpressure. Particular focus should be drawn to the conclusion that, in this

instance, obstacles can have both positive and negative impacts on the peak overpressure, depending on the point of interest’s location relative to the blast and surrounding obstacles.

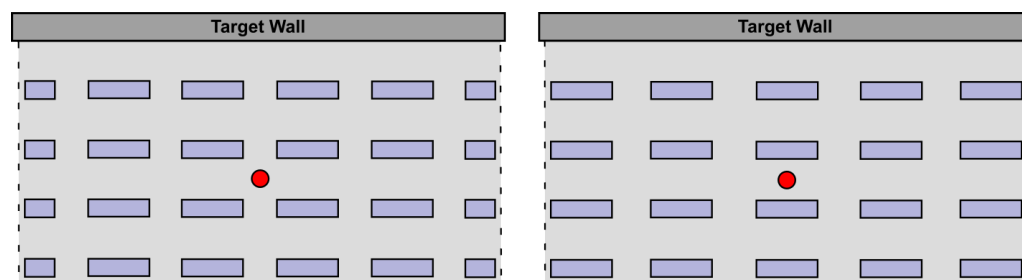


**Figure 2.** Diagram showing plan views of the channelling (left) and shielding (right) type layouts used within the Air3D simulations. Red circles highlight the charge location. Adapted from Smith et al. [37].

These findings may be beneficial in grid-type-layout cities, such as those commonly found in the USA [39]. However, many other non-grid-layouts need consideration. Smith et al. [37] also conducted simulations using random arrays of buildings with varying areal densities, either featuring direct or non-direct paths from the explosion origin to the wall. The sum of the impulse measurements from a given configuration were compared to an equivalent “no obstacle” scenario, termed the shielded and unshielded value, respectively. This process was repeated for several layouts, with the shielded impulse loading relative to the unshielded loading for a given areal density summarised in Table 1.

**Table 1.** Reduced loading due to shielding on a target wall from blasts contained within random arrays of varying building areal density. Note: 93.5% shows that the average impulse along the target wall was 93.5% of the unshielded value—a 6.5% reduction, adapted from Smith et al. [37].

Areal Density	Impulse Reduction	
	Direct Line	No Direct Line
28.6%	93.5%	87.5%
22.0%	88.8%	88.2%
17.9%	85.1%	86.6%
Average	89.1%	87.4%

The results in Table 1 suggest that an increased areal density lessens the protective shielding elements of the various building arrays when there is a direct line of sight from the blast origin to the target wall. This is described as being “perhaps rather counter-intuitive” as it was initially expected that an increased areal density would reduce the loading experienced on the wall. It is stated that a “combination of shielding and channelling” produces these results [37]. It was posited that the increased areal density worsens the effects of channelling more than the protective effects of shielding, so an increase in loading is seen. An optimal areal density may exist where the shielding element is maximised and the channelling element minimised. Additionally, it could be argued that the “no direct line” results do not appear to follow any relationship from the data presented. The characterisation of an urban layout in the form of areal density may be too simple and too great a reduction of the underlying physics to develop meaningful loading predictions from. The key factors governing this have yet to be identified, either numerically or experimentally.

In a related study, Smith et al. [40] investigated the shielding effects of houses. A terraced and detached layout was constructed with concrete beams and blocks. Results from both layouts suggested that “the presence of a building between the explosion and the “target” building produced a shielding effect and the blast resultants were reduced compared to the situation where there was no intervening building”. This generally agrees with the findings from Smith et al. [37] as discussed above. However, Smith et al. [40] showed that the most effective form of shielding occurred when the buildings were near each other, tall, and relatively

large compared to the explosive mass used. Whilst this conclusion can be taken from this study, it could be perceived as contradicting the findings from Smith et al. [37], where increasing the areal density resulted in less effective shielding. However, this discrepancy cannot be assured; the building height is not accounted for in Smith et al. [37], and the building layouts differ between the studies. As a minimum, it could be logical to assume that the areal density, specific layout, and building heights should all be considered in predicting urban blast loading. An additional conclusion from Smith et al. [40] was that the blast interaction with the first row of buildings was the most important factor regarding the shielding effect of the blast compared to other rows of buildings. This was later confirmed by the modelling work of Gan et al. [41], described in Section 3.3, who found that channelling dominated closest to the charge and hypothesised that channelling is a localised effect, whereas shielding is cumulative.

#### 2.4. Effects of Street Confinement

Fouchier et al. [42] explored blast wave propagation within modelled street environments. Specific layouts selected for testing include a straight street, a T-junction and a cross junction. An explosive bridge wire detonator, type RP80, was used to create equivalent, small-scale free air blasts. It was seen that an increase in overpressure persists out to greater distances when the confinement of a street is present, compared to a free-air scenario; similar findings were reported by Smith et al. [43]. However, the increase in overpressure is not seen at shorter-scaled distances. Instead, it is seen to be similar to the overpressure experienced in a free-field scenario. Figure 3 shows a sample of these results and is also supplemented with additional reference curves from free-field hemispherical TNT surface blast tests from Kinney and Graham [44] and France groupe d'étude des Modes Operatoires (GEMO) [45].

This behaviour is described as a result of the reflected shock wave not yet merging with the incident shock wave. Instead, a pressure sensor reads two peaks, where the amplitude is similar to that of a free-field blast. Therefore, the scaled impulse was used to quantify blast loading at smaller-scaled distances within wider street widths.

In addition to the street width and shape, the confining building height was also considered. It was found that the height of the buildings also alters the blast characteristics. In the case of a tall street, the blast parameters are enhanced as the blast's energy is more contained. A taller street will consistently experience larger pressures and scaled impulses compared to a shorter street of the same width and shape.

Channelling effects through an array of buildings were also explored; the array sizing was  $4 \times 4$  and slightly rectangular (skewed in the longitudinal direction). It is stated that *"between the spaced buildings that decrease the blast characteristics and the confinement that increases them, the blast characteristics are similar to a free-field propagation"*. Whilst this statement is made, closer inspection reveals that impulse data within the array is slightly reduced compared to free-field data. This could be linked to the behaviour characteristics of shielding and channelling "somewhat mitigating" each other in Smith et al. [37], but overall resulting in a small reduction of impulse. However, it is seen that once the blast exits the array, the pressure and impulse experience an 80% reduction compared to a free-field scenario. This could suggest that global energy loss of the shock wave occurs as it propagates through an array, but the confining effect of the array largely compensates for this energy loss. It is only when a shock wave propagates beyond an array that the energy loss is significantly shown in the reduction of the pressure and impulse.

Rose and Smith [46] numerically and experimentally investigated blasts within straight streets. Model streets were constructed out of concrete blocks and beams that formed a set of parallel walls. The walls acted as building façades where multiple pressure transducers were installed. Initially, experimental and numerical results showed good agreement, validating the use of Air3D for the remainder of the study.

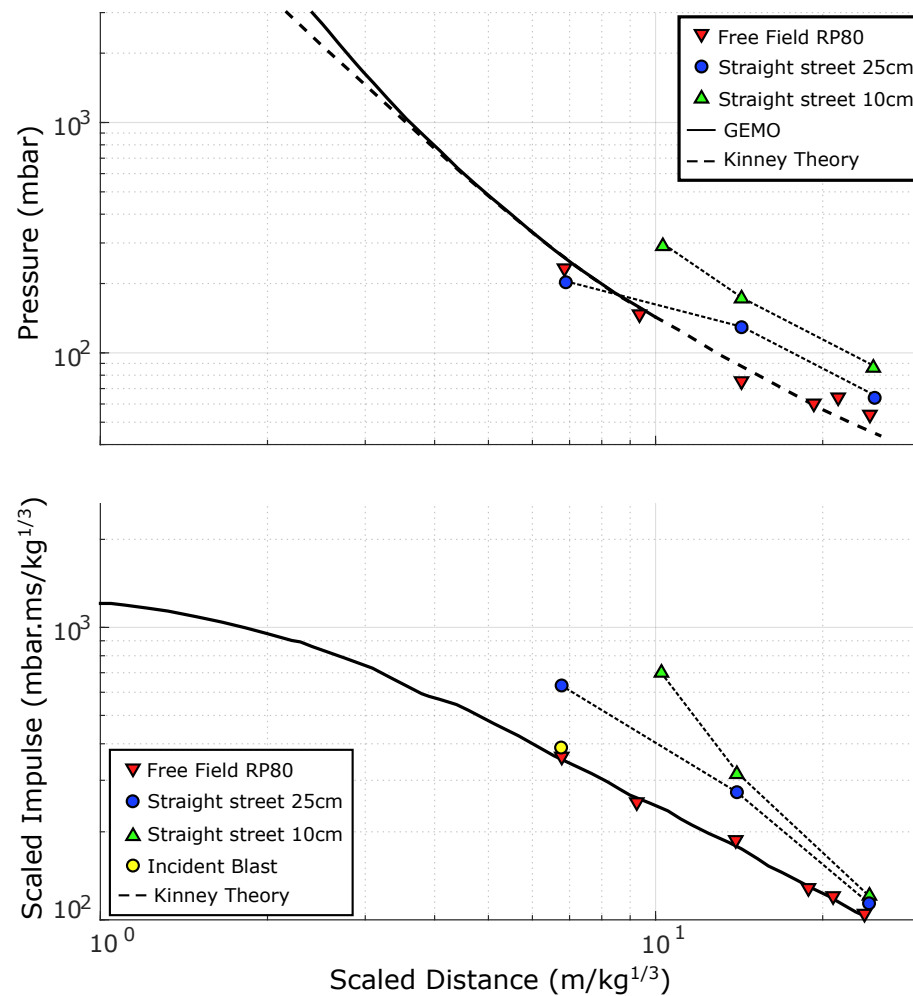


**Figure 3.** Plots showing pressure and impulse data measured for various street widths (10 cm and 25 cm), supplemented with free-field data from an RP80 and theoretical curves for a free-field scenario, adapted from Fouchier et al. [42].

The numerical investigation found that the smaller street widths and taller building heights increased the positive phase impulse for the same explosive mass. It was also found that a scaled street width of  $4.8 \text{ m/kg}^{1/3}$  can be considered the limit where reflections from one side of the street do not affect the loading on buildings at the other side of the street. Additionally, in observations that were later ratified by Fouchier et al. [42], it was seen that larger building heights also increased the scaled impulse for the same explosive mass. A building height of  $3.2 \text{ m/kg}^{1/3}$  or greater can be considered “infinitely tall”. Whilst this is a reasonable assumption, there is still some discrepancy in the scaled impulse results between an “infinite” and  $3.2 \text{ m/kg}^{1/3}$  building height at larger scaled distances along the street, suggesting this limit might be slightly too low.

### 2.5. Degree of Confinement

Ripley et al. [47] also explored the effects of urban confinement on blast loading. They defined the near-field as a “range where scaling rules do not apply” and state that this regime extends further when urban confinement is present. This is termed the “extended near-field regime” and typically extends to larger-scaled distances for wider streets. Regarding pressure, in the case of a straight street, the “extended near-field regime” exists within the scaled distance where primary reflections have not yet merged with the incident blast wave. Maximum overpressures on structures within this space did not change in magnitude

compared to a singular-walled scenario; only impulse enhancement was generally seen to occur. This agrees with the blast wave behaviours discussed in Fouchier et al. [42].

Beyond the scope of the near-field regime within straight-street tests, significantly greater overpressures were present compared to a free-field scenario. This occurs due to the street-reflected and incident blast waves combining to form an ultimately stronger blast wave, a phenomenon otherwise termed “blast wave coalescence”. The magnitude of this increase was greater for a narrower street than a wider one, assuming the street is suitably long for coalescence to occur. It was also seen to occur at a shorter distance for a narrower street compared to a wider street; all scenarios assumed the same explosive mass was used.

Ripley et al. [47] also examined the afterburning effects of the detonation products. *“Afterburning occurs when fuel-rich explosive detonation products react with oxygen in the surrounding atmosphere. This energy release can further contribute to the air blast, resulting in a more severe explosion hazard, particularly in confined scenarios”* [48]. Indeed, increases in overpressure and impulse were prevalent for all street widths tested. These effects were attributed to increased fireball temperature and size, resulting in the acceleration of blast reflections. Metallised TNT was seen to enhance these effects further.

A new parameter was proposed, termed the “degree of confinement”. It is described as a quickly-attainable metric that can determine the potential extent of urban environment effects on average scaled impulse for a given urban blast. Equation (3) details the basic formula, which includes a closed-area “wall ratio” and a “corner ratio”. These ratios are defined in Equations (4) and (5). As seen in Equation (3), these ratios are weighted equally, although it is stated that further refinement of the general concept is required.

$$DC = (WR + CR) / 2 \tag{3}$$

- WR is the wall ratio.
- CR is the corner ratio.

$$WR = \frac{\sum_i^r H(Z_{\text{cutoff}} - Z_i) A_i Z_i^{-1}}{\sum_i^{\text{all}} A_i [\min(Z_i, Z_{\text{cutoff}})]^{-1}} \tag{4}$$

- H is a Heaviside function (returns 1 if positive or 0 if negative).
- $Z_{\text{cutoff}}$  is the limiting scaled distance ( $\text{m}/\text{kg}^{1/3}$ ).
- $Z_i$  is the scaled distance to the  $i^{\text{th}}$ -reflecting surface ( $\text{m}/\text{kg}^{1/3}$ ).
- $A_i$  is the area of the  $i^{\text{th}}$ -reflecting surface ( $\text{m}^2$ ).

$$CR = \frac{\sum_i^c c_i Z_i^{-1} H(Z_{\text{cutoff}} - Z_i)}{\sum_i^{c, \text{max}} c_{\text{max}} [\min(Z_i, Z_{\text{cutoff}})]^{-1}} \tag{5}$$

- $c_i$  is the corner factor and has pre-defined values depending on the corner type.
  - Ground diffraction corner,  $c = 2$ ;
  - Top of building diffraction corner,  $c = 1$ ;
  - Ground re-entrant corner,  $c = 4$ ;
  - Top of building re-entrant corner,  $c = 4$ .

The utility of the degree of confinement concept was tested by analysing a set of scaled urban blasts. It was seen that the degree of confinement parameter generally produced values as expected: the most confined scenario returned the highest degree of confinement. Cylindrical and spherical charges of the same mass were used, and the average scaled impulse measured across multiple sensors was plotted against the degree of confinement.

A reasonable logarithmic relationship was apparent between the variables; see Figure 4, adapted from Ripley et al. [47].

The results in Figure 4 suggest that blasts within more confined urban settings will produce greater loading more often than not. Anthistle et al. [49] found a similar characteristic, where the peak impulse was shown to increase along a “quarter symmetry wall” when obstacles were present, compared to a no-obstacle scenario. Likewise, a similar behaviour was observed by Sochet et al. [50], where overpressure increased with confinement, although this confinement is not quantified, but visually shown instead. This could also agree with what is seen in Smith et al. [37], where larger areal densities increased the average impulse measured on a target wall, but this is only relevant for a small sample and range of areal densities with a direct line from the blast to the target wall. Furthermore, the findings by Ripley et al. [47] also contradict what is reported by Fouchier et al. [42], where the scaled impulse decreases slightly within a confining array. A direct comparison cannot be made as the input metrics are not the same, but it can be said with reasonable confidence that there exists a gap in the knowledge, which requires further investigation.

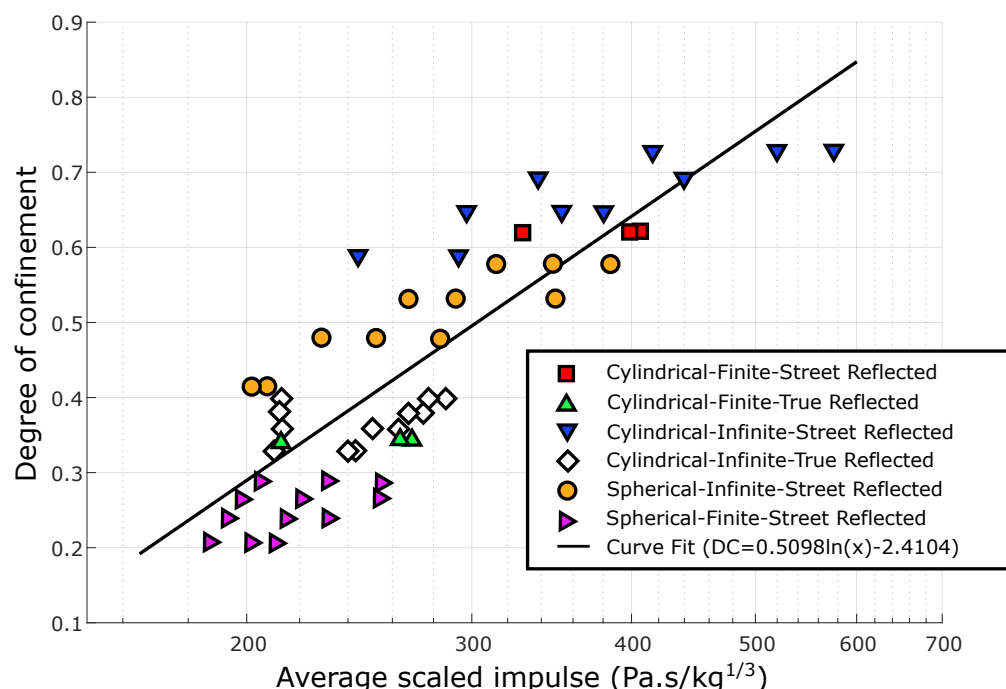


**Figure 4.** Plot of the degree of confinement vs. average scaled impulse for multiple urban street tests, adapted from Ripley et al. [47].

The degree of confinement metric has since been explored further using a largely numerical basis [51]. It was acknowledged that the first iteration of the degree of confinement was limited in that “it becomes very difficult to compute for more complex, real-world urban environments”. Likewise, in its previous form, the method did not “lend itself to incorporation into automated software”. For these reasons, a refined approach was determined. The geometry is first discretised into a 3D mesh, with a mesh resolution size of 0.1 m/kg<sup>1/3</sup>. A confinement region extends outwards from the charge position until it reaches a structure or a  $Z_{\text{cutoff}}$  of 6 m/kg<sup>1/3</sup>. This region can “wrap” around structures to points outside the line of sight relevant to the charge. The weighted “open” and “closed” areas,  $A$ , are then calculated based on the cut-cell areas between the structural elements and the mesh. The inverse distance of each cut cell to the charge is also accounted for,  $D^{-1}$ . The revised calculation for the degree of confinement is shown in Equation (6).

$$DC = \frac{\sum_i^{closedcells} (AD^{-1})_i}{\sum_i^{allcells} (AD^{-1})_i} \tag{6}$$

- $A$  is the cut cell area.
- $D$  is the inverse distance of each cut cell from the charge.

To incorporate a range of charge masses for the relationship between the degree of confinement and blast loading, a metric termed the urban blast load (UBL) was used. The UBL is a function of the charge mass and the total walled area loaded from the blast, which falls inside  $Z_{cutoff}$ . The UBL is defined in Equation (7), where  $I_{total}$  is defined in Equation (8).  $I_{total}$  is described as the sum of the max impulse values for any given cell at a structural boundary, divided by the total area of the structural boundary. The UBL displays an improved correlation (see Figure 5) between blast loading and the degree of confinement compared to that found in [47]. Although a relationship is not quantified, visually, it is evident that a nonlinear fit is appropriate.

$$UBL = \frac{I_{total}A_{wall}}{W_{TNT}} \tag{7}$$

- $A_{wall}$  is the total wall area loaded by the blast (within  $Z_{cutoff}$ ).
- $W_{TNT}$  is the TNT equivalent charge mass.
- $I_{total}$  is the average maximum specific impulse across all cells at a structural boundary (Equation (8)).

$$I_{total} = \frac{I_{max}A_{wall}}{W_{TNT}} \tag{8}$$

- $A$  is the cut cell area.
- $D$  is the inverse distance of each cut cell from the charge.

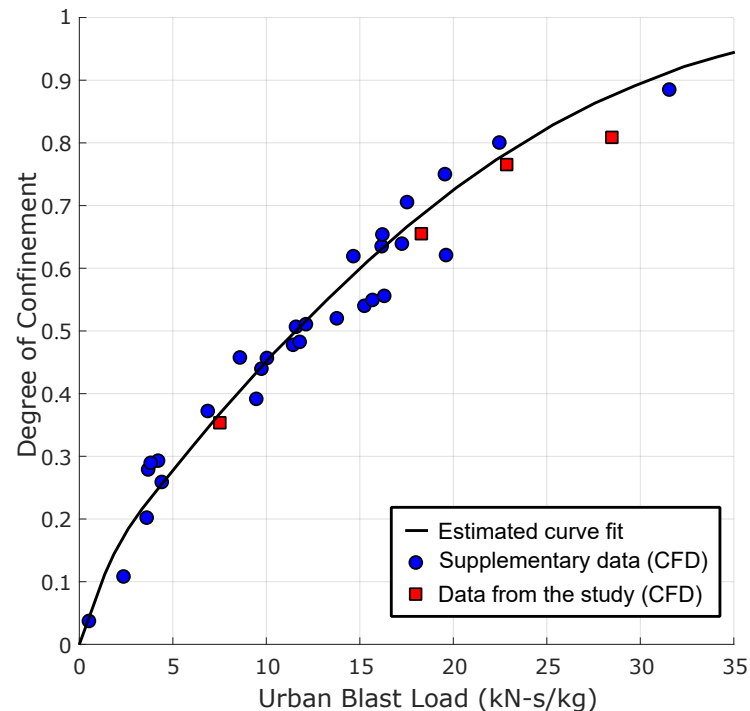


Figure 5. Revised Degree of Confinement vs. Urban Blast Load, adapted from Donahue et al. [51].

### 2.6. Façade Failure

Smith et al. [52] conducted a study where the effects of façade failure were explored. An experimental model was constructed of a long, straight street at a 1:50 scale. Varying percentages of façade gaps were created, termed as the porosity, ranging between 24–77%. It was shown that impulse (measured down-street) decreased in an approximately linear fashion as the porosity increased. This would seem logical, as gaps in the façade would reduce the confining effect of the street. The study was extended using numerical methods (Air3D) to examine the impact of façade failure inside the building. It was found that if a blast could penetrate a building, the resultant loading could cause damage to both the occupants and the building fabric. Ultimately, it was concluded that façade failure is undesirable, so building fabrics should be sufficiently designed to be as robust as reasonably possible. It was argued that it is better to have a larger quantity of buildings damaged externally than fewer buildings damaged internally where more civilians tend to reside.

Dib et al. [53] explored the shielding capabilities of buildings with varying porosity levels in regard to overpressure measured on a virtual façade situated downstream of the blast. Relatively high-yield blasts (300 tonnes of TNT) were numerically modelled at three different stand-off distances from the porous building: 50 m, 150 m and 450 m. The distance between the porous building and the façade was increased in increments of 5 m between simulations. Four different porosity levels were defined as zero, low, medium and high, with façade porosities of 0%, 38%, 54% and 100%, respectively. The results show that, generally, shielding effects are enhanced with shorter stand-off distances between the explosive and the “protective” building; this is in agreement with the findings from Smith et al. [40].

The zero- and low-porosity buildings provided some form of shielding for all combinations of the stand-off and the gap between the protective building and the façade. Likewise, the medium-porosity building reduced the average overpressure on the façade when the gap was less than 40 m, rarely performing better than the lower porosity levels. However, it should also be acknowledged that the 100% porous building had little effect on the overpressure measured on the virtual façade for the 150 m and 450 m stand-off distances compared to a free-field scenario. Additionally, minor overpressure enhancement for the 50 m stand-off distance was shown to occur when the gap between the building and the virtual façade was 40 m or less. The findings here suggest that care should be taken when predicting blast loads on secondary surfaces behind porous protective elements, as mitigation effects are not always prevalent.

### 2.7. Surface Roughness

Dewey et al. [54] compared the behaviour of shocks reflected from both real and ideal surfaces. The ground was used as a real surface, and to simulate an ideal surface, the shock was reflected off the shock from an identical explosive mass placed above the initial explosive and simultaneously detonated. It was stated that there is no energy loss from the interaction of the two shock waves, allowing this interaction plane to act as an “ideal non-energy-absorbing surface”. A key finding from this study was the change in peak overpressure measurements from the Mach stem over rough ground compared to the ideal surface. Simplified, the Mach-stem shock caused by a 1 kg explosive over rough ground would equate to that from a 0.74 kg explosive over an idealised reflecting surface. Whilst the roughness of the ground was not explicitly defined, it can be stated that any non-ideal reflecting surface will result in energy losses that may be significant, and therefore should be accounted for in numerical simulations. The relationship between the values of surface roughness and energy loss would prove useful for numerical models and improve their accuracy. Others have accounted for these energy losses by adopting a “local flow resistivity” approach by altering model coefficients for varying local roughness [55].

### 2.8. Large Magnitude Urban Blast

On 4 August 2020, one of the largest non-nuclear explosions in history occurred in the Port of Beirut, Lebanon. Approximately 2750 tons of ammonium nitrate, which had

been held in storage since 2014 [56], detonated shortly after 18:07 local time following a fire in the warehouse where it was being stored. The explosion injured over 7000 people and resulted in more than 200 casualties and over \$15 billion in infrastructure damage [57]. Broken glass and debris were observed at distances up to 3 km away, encompassing an area with more than 750,000 inhabitants [58].

Rigby et al. [4] estimated the yield of the explosion using video footage uploaded to social media shortly after the event. In total, 38 individual data points were identified, and a mixture of fireball, audio and visual data was collected. By searching through the videos on a frame-by-frame basis, the time of detonation and the time of arrival could be determined. By identifying a video's recording location, the distance to the blast origin could be approximately determined ( $\pm 10$  m) through Google Earth.

The authors derived a simplified polylogarithmic function based on the Kingery and Bulmash [59] semi-empirical relationships for the time of arrival as a function of scaled distance. A "best fit" yield range was determined to be 0.50–1.12 kt of TNT, as shown in Figure 6. It should be noted that the best estimate was 0.50 kt TNT; the upper limit of 1.12 kt of TNT was given to account for the significant uncertainties in the raw data. Stennett et al. [60] adopted a similar approach to Rigby et al. [4], albeit with a smaller number of datapoints, and estimated the yield to be  $\sim 400$ –960 tonnes TNT equivalent. This suggests that, for large-magnitude explosions, time and distance data are sufficient to obtain a reasonable and rapid estimate of the yield—even when the dataset is relatively coarse.

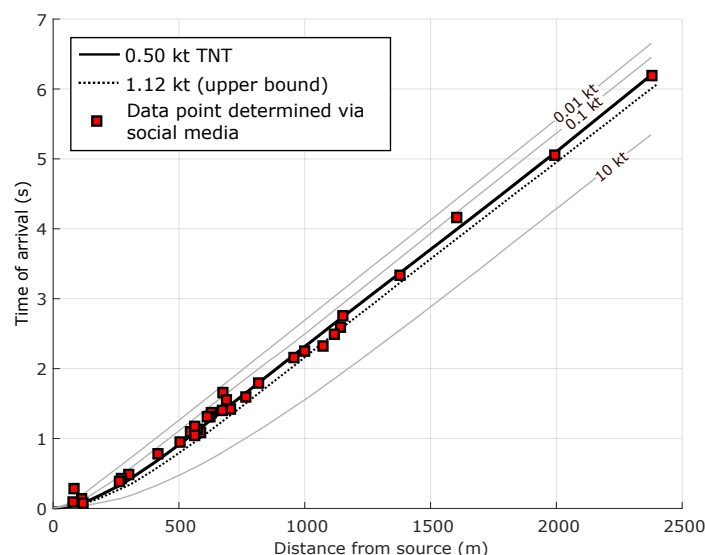


**Figure 6.** Best fit yield of the Beirut explosion with an upper yield, adapted from Rigby et al. [4].

Other approaches, e.g., dimensional analysis of the detonation product fireball [61–63], the Locking [64] power index method [65], analysis of seismological, hydroacoustic, infrasonic and radar remote sensing data [66], observed damage to structures [67–69], crater size [70], and debris/mushroom cloud height [71], generally agree that the yield of the Beirut explosion was in the range of 200–1400 tonnes TNT equivalent.

The events in Beirut are not unprecedented; there have been many recent large scale industrial explosions ( $\gg 10$  tonnes TNT equivalent) in built-up areas [56], including Tianjin, China (2015; 173 deaths), and Buncefield, UK (2005; 43 injuries). Accordingly, the structural response to long-duration blast loading is an ongoing topic of interest, particularly for structures sensitive to such loads, e.g., bare steel sections [72,73], partially-clad steel frames [74], cylindrical shell structures [75,76], ISO containers [77], and bridges [78]. Accurately simulating long-duration blasts and their interaction with structural components several times smaller than the blast wavelength is highly challenging and requires considerable computational expense [79,80].

## 2.9. Alternative Protective Methods

Warnstedt and Gebbeken [81] explore alternative solutions regarding blast protection that are not easily identifiable as protective methods. They focussed their research on studying the pressure-reducing effects of Bamboo, Barberry, Thuja and Yew trees. The experimental set-up consisted of a 5 kg TNT equivalent explosive at a 5 m stand-off distance from the various plants. This mass was chosen as it was within the range of an explosive mass that could be carried inconspicuously by an individual. Overpressure time histories were measured by pressure sensors (type 113B28, PCB Piezotronics) with a sampling rate of 1 MHz. A tri-axis arena was set up to allow for the simultaneous testing of multiple plant types.

The results showed that peak overpressures were in good agreement; however, the impulse values did not correspond to the expected values. This was attributed to the shape of the pressure sensor housing. It was determined that the pressure sensor used meant that the impulse migration effects of plants could not be assessed further. Significant pressure reductions were seen in the areas behind the Thuja and Yew trees at 39% and 45%, respectively. It was noted that little biomass was removed from these plants due to the blasts, indicating that continued protection is possible from repeated blast events. In contrast, the Bamboo and Barberry plants achieved an initial pressure reduction of 30% each, but a large proportion of the biomass was removed, thus reducing the protective properties from repeated blasts. It was concluded that all plants tested offered some form of protection compared to an open-air scenario, but needle-type plants proved to be the better form of natural defence.

It has been shown that single obstacles [82] and an array of multi-scale (pre-fractal) obstacles [83] can lead to considerable blast wave attenuation through shock disruption and vortex shedding. Up to 14% and 26% reductions in loading were seen for the single and multiple obstacles, respectively. For a more comprehensive review of blast–obstacle interaction, the reader is directed to Isaac et al. [84].

## 3. Numerical Methods

### 3.1. General Computational Fluid Dynamics Studies

CFD (computational fluid dynamics) numerical models gained particular traction for blast applications in the early 2000s [85,86]. Obtaining reliable and precise outputs from CFD simulations typically comes at a high computational cost [87]; however, CFD is becoming an increasingly attractive and cost-effective research tool [88–91].

Numerical simulations have previously been used to study blast propagation in simple urban areas with some success [92,93]. Luccioni et al. [94] and Ambrosini et al. [95] determined the equivalent mass and location of the explosive device used in the 1994 Buenos Aires terror attack by correlating the observed damage with the loading distributions from a range of numerical analyses in a congested urban environment. In a similar study, Christensen and Hjort [96] used numerical analysis and simple structural response models to back-calculate the yield of the 2011 Oslo bombings. Marks et al. [97] conducted a probabilistic assessment of blast loading to determine fatality risks due to the pressure and impulse from a vehicle-borne improvised explosive device detonated at a T-junction in an urban streetscape, an extension of the work to determine fatality risks due to the detonation of an improvised explosive device inside a typical ground floor lobby of a large commercial or government building [98].

Valsamos et al. [99] analysed the impact of the 2020 Beirut explosion using CFD. A combination of geospatial data (a type of data used for other urban blast studies [100]) and CAST3M software was used to produce a finite element model of the cityscape for use within the numerical analysis. Such a replication was described as being able to “incorporate with great accuracy all the important geometric details of the buildings in an urban environment”. It should be noted that the phrase “great accuracy” is relative to the model’s size. Upon closer inspection, the model is coarse (compared to models employing 10 s–100 s kg high explosive), with an average mesh size of 5 m. Additionally, small or mobile structures were

omitted from the model as they were considered insignificant. Structural details are also limited as a consequence of the mesh sizing used. Understandably, these limitations were adopted to reduce the computational cost of the analysis, but their significance to the final solution remains unknown. It is explained that decreasing the size of the finite volumes “does not really change the solution”, but this change is not quantified.

The research claims that CFD-based simulations are necessary to reflect, more truly, the behaviour of shock waves in geometrically complex settings—agreeing with earlier claims in the field [101]. Effects such as channelling, shielding and interference from multiple wavefronts can be simulated in this computationally expensive method, leading to greater accuracy in the results. This combination of tools can facilitate the calculation of long-duration blast effects with reasonable accuracy regarding the consequences of a large-scale blast event, provided the origin and yield are known.

### 3.2. Eagle-Blast

Cullis et al. [102] utilised EAGLE-Blast to simulate geometrically complex blast scenarios. EAGLE-Blast is a blast-specific simulation software that acts as a module, which can be inserted into a larger software package named EAGLE. The addition of the EAGLE-Blast module allows for the inclusion of rigid elements contained in the flow field and is especially “tailored for blast simulations”. The paper contains multiple studies showcasing the modules’ ability to perform simple blast simulations. It states that the results “offer confidence that EAGLE-Blast can capture shock propagation and interaction reasonably well”. However, due to the approximation nature of the software regarding the ignition and detonation of an explosive, only the relatively far-field behaviour blast effects can be captured with reasonable accuracy.

The EAGLE-Blast module’s suitability in conducting geometrically complex blast simulations is demonstrated through a comparison and validity study. Experimental modelling results from 1:50 scaled blasts were utilised as a basis for the comparison [103]. The simulated overpressures were recorded at the same locations that housed pressure sensors in the experimental model for a direct comparison. The paper does not present all the data, but the results from four pressure sensors for a given charge location are shown in Figure 7. A good correlation is present between the experimental and numerical data. Minor discrepancies were pointed out, but their cause is not certain. They are described as a potential consequence of the measurement fidelity or afterburning effects not being simulated within EAGLE-Blast at the time of writing.

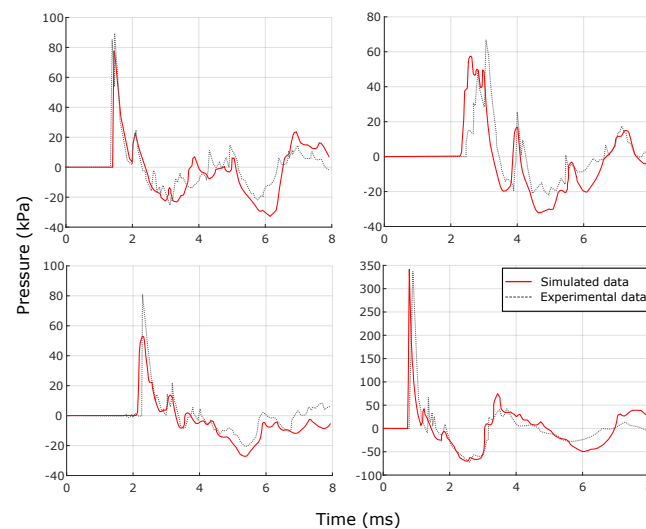


**Figure 7.** Pressure vs. time plots comparing experimental and simulated data for a set charge location at four different pressure sensors, adapted from Cullis et al. [102]. Note: The paper does not state which pressure sensor is associated with each plot.

### 3.3. BlastFoam

Gan et al. [41] utilised BlastFoam, an open-source computational software, to investigate blast wave interaction with randomly positioned objects inside a crowded environment. The positioning of obstacles was not truly random in all tests; a predetermined bias (towards or away) was selected to allow for some form of controlled input—though the positioning of obstacles was still random within the bounds of the bias. Compared to the no-bias scenario, the object bias towards the blast increased the blast loading towards the centre of the domain while reducing the blast loading towards the outside of the model. The opposite can be said when the bias is away from the centre, see Figure 8. These results could be linked to the shielding and channelling behaviours discussed in Section 2.3, where the two are seen to somewhat counteract one another. BlastFoam compares well against other CFD-based software used within the field and has been previously validated in numerous cases [104,105].

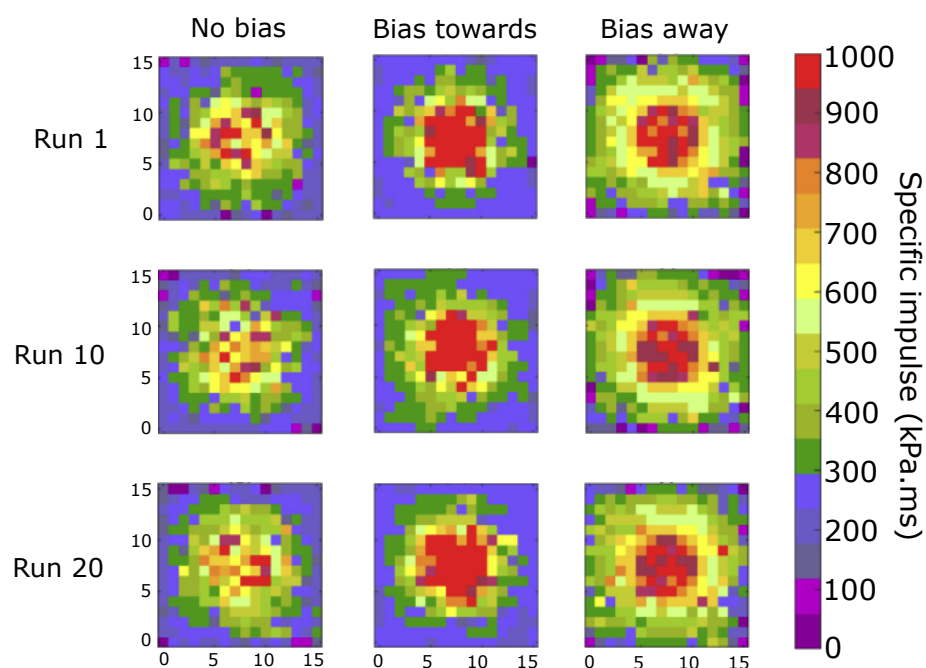


**Figure 8.** BlastFoam simulated peak-specific impulse data for different predetermined object location biases at multiple numbers of test runs, adapted from Gan et al. [41]

### 3.4. BeamBlast

Halswijk [6] describes the development of a new module to be used in blast simulations named BeamBlast. The module aims to find a middle ground between semi-empirical methods and CFD analyses to balance simulation speed and accuracy. It is specifically for use in “Military Operations in Urban Terrain” (MOUT) scenarios, where such attributes of the module are desirable. The module runs within a wider simulation software suite known as “Target Vulnerability Assessment Code” (TARVAC), which is generally used to determine the lethality of ammunition required for destroying a given target. BeamBlast also aims to provide a fast-running path-based blast propagation model, which requires limited user input.

The module implements path-finding algorithms that identify paths from a blast origin to a specified location of interest, taking surface and edge interactions into account. Afterwards, the pressure and time data are calculated for a given set of paths and explosive masses, based on the Kingery and Bulmash relationships [59]. Initial validations were conducted using simple rectangular models that represented street buildings. The numerical data were compared to experimental data [106], and simulations were run at three different levels of complexity. The simplest simulation measured pressure and impulse on

a building wall directly opposite the blast. The intermediate simulation measured pressure and impulse on the side face of the same building. The complex simulation measured the pressure and impulse on the ground at the rear of the building.

In the simplest scenario, BeamBlast demonstrated relatively good agreement with experimental pressure data throughout the test duration. The impulse data were seen to drift slightly, although this was attributed to problems with an offset correction. The results from the intermediate and complex scenarios also exhibited relatively good agreement with the experimental data, but deviated later on, after approximately 10 ms. The main concluding remark regarding BeamBlast was that “it is capable of reproducing the propagation of relatively weak blast waves around rectangular obstacles up to a few blast time lengths”. The deviations in the complex scenario data set may suggest that BeamBlast struggles to replicate blast behaviour in the later stages after detonation accurately—potentially due to the cumulative errors from multiple blast wave interactions. Additional updates were planned for the software in 2015, and further review is required to analyse the sophistication of BeamBlast in the present day.

### 3.5. Mm-Ale Solver

Lee et al. [107] present a blast pressure prediction model that utilises the Multi-Material Arbitrary Lagrange-Eulerian solver (MM-ALE) in LS-DYNA. Typically, this approach is restricted to the analysis of near-field scenarios, as the MM-ALE solver requires a rapidly increasing number of elements for larger configurations. To enable the testing of larger configurations, 1D to 2D to 3D mapping was used to reduce the computational cost considerably. This approach does not compromise the results compared to those obtained using the same mesh sizing without mapping. Furthermore, it can allow for greater accuracy in the prediction of peak pressures via the use of denser mesh sizing.

Experimentally obtained results [108] were compared to the numerical results from the MM-ALE analysis, see Table 2. It is seen that both sets of results are comparatively similar. A few data pairings contain some variations from each other, but these were somewhat overlooked. By using mean values, the approach was validated and “shown to achieve accuracy”; however, it is only computationally feasible for symmetric situations. Lee et al. [107] went on to develop a fast-running blast model through the use of regression analysis to rapidly estimate peak overpressures acting on buildings following the detonation of explosive devices in typical urban street configurations (dead-end and cross-road), taking inputs such as street width, explosive mass, and location. This approach was validated using the simulation results found earlier in the study.

**Table 2.** Comparison of experimental and numerical peak pressure data [107]. Note: Sensors H1, V1 and D1 are the same sensors.

Pressure Sensor ID	Analysis (kPa)	Experiment (kPa)	Percentage Difference
H1	2324	2281	1.9%
H2	782	728	6.9%
H3	398	312	21.6%
H4	303	224	26.0%
V1	2324	2432	−4.6%
V2	1310	1272	2.9%
V3	723	472	34.7%
V4	359	252	29.8%
D1	2324	3613	−55.5%
D2	920	921	−0.1%
D3	505	402	20.4%
D4	332	238	28.3%

### 3.6. Neural Networks

In general terms, neural networks are computational-based models whose architecture and function are said to be “loosely inspired by the human brain” [109]. They consist of an

assembly of many “highly connected processing units”—termed the nodes or neurons [109]. The nodes are connected via unidirectional communication channels, which have individual weightings attributed to them. The weightings dictate the strength of a given connection, and knowledge storage is achieved in the form of collected weighting values. Nodes activate based on threshold values, which are functions of the sum of the inputs received from other nodes. Collectively, this allows a neural network to learn, which enables sought-after characteristics such as the capability to produce outputs when presented with an incomplete set of inputs. Furthermore, neural networks can apply a certain level of generalisation provided by the database from which they are trained—typically, this would be known input–output pairs. Training rules can be implemented that adjust the weighting of connections so that a model can obtain the desired outputs within a specified tolerable accuracy (usually 5 to 10 %).

Remennikov and Mendis [109] explored the prediction of blast loads in urban streets from a bomb detonation using neural networks. A database consisting of 49 individual analyses of a blast within a straight street from CFD blast simulations (Air3D) was used to train and validate the neural network; NeuroShell 2, Release 4.0 in this case. Peak impulse and pressure data were treated as the outputs of the configuration. Multiple neural networks were produced, each with a unique network configuration. The network that showed the least absolute mean error between the expected and estimated outputs was selected.

The outputs from the neural network are stated to show “very good agreement with those obtained from the CFD simulations”, with the positive impulse values receiving a particular mention as being “very close” (see Figure 9, adapted from [109]). A closing remark states “it has been proven that a neural network can be used as an effective tool for rapid prediction of blast effects in urban environments”. Whilst this seems to be the case presented by Remennikov and Mendis [109], it should be noted that the geometries of the neural network models were the same as the database models. It may be more appropriate to say that neural networks can be used as an effective prediction tool, provided they are suitably trained using a thorough dataset to improve performance, similar to a conclusion determined by Dennis et al. [110]. Likewise, Ruscade et al. [111] use data-rich experimental work (30 pressure vs. time data sets per test) for the training of a numerical model, although no further detail is provided about the model.

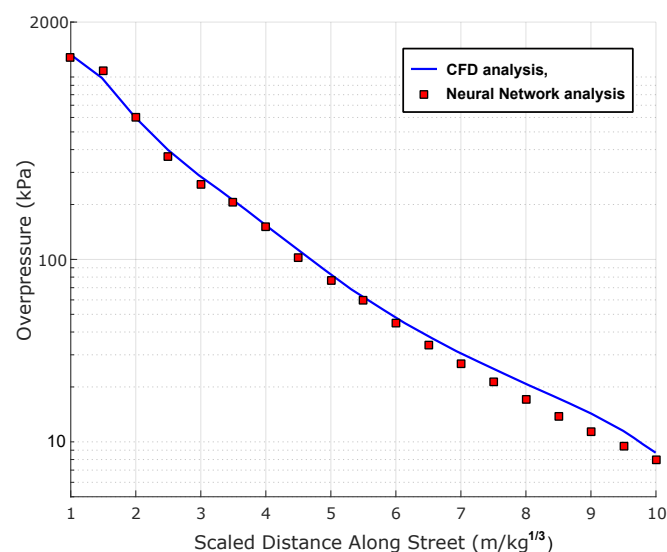


**Figure 9.** Neural network and CFD overpressure outputs for a straight street blast, adapted from Remennikov and Mendis [109].

Other blast-related applications of data-driven [112,113] and neural network-based predictive approaches [114–116] have been shown to have highly favourable computa-

tional times compared to CFD simulations. Flood et al. [117] showcased a neural network that was capable of running as much as six orders of magnitude faster than a CFD simulation for a 3D scenario, with similar results reported by Kang and Park [118]. Zahedi and Golchin [119] also compared neural network-based modelling to CFD simulations and stated that their results “*demonstrate the potential for machine learning algorithms to revolutionise CFD analysis for blast loading*”.

## 4. Experimental Methods and Instrumentation

### 4.1. Imaging Techniques

#### 4.1.1. Three-Dimensional Imaging

Winter and Hargather [120] used background-orientated schlieren (BOS) to reconstruct three-dimensional shock waves using multiple high-speed cameras pitched at varying viewing angles. BOS is a detection method that allows for the visualisation of shock waves and is termed a refractive imaging technique. The increased density at a shock wave boundary increases the refractive index of a given fluid at that location. Using a suitable background with high spatial frequency and contrast makes it possible to capture a distortion against the background using a high-speed camera. Therefore, a shock front's subsequent location can be determined by identifying this distortion's location. There are numerous approaches to processing these images; most use a reference image and a “distorted image”, followed by a type of comparison. BOS is described as an “*effective method to visualise explosively driven shock waves*”. Two common methods include image subtraction and image correlation, both of which have been widely used or discussed in other sources, e.g., [121–123]. Alternatively, optical flow tracking velocimetry methods [124] may be used.

Winter and Hargather collected a series of images using four high-speed cameras using image subtraction processing techniques to form BOS images. The development of an automatic point detection algorithm allowed for the location of shock waves to be determined efficiently. The algorithm's point detection capabilities were tested against a “careful” manual detection and were shown to achieve good accuracy. As a result, it was revealed that these techniques could define the three-dimensional shape and size of a given shock wave. Whilst this technique could track both spherical and asymmetric shock waves, its feasibility was only tested within the boundaries of a simple scenario. When used within a scaled experiment for an urban setting, the inherent complexity from numerous shock reflections may prove more challenging to capture. Additionally, the careful placement of cameras would need to be considered to minimise or eliminate potential blind spots.

#### 4.1.2. Schlieren Imaging

Dela Cueva et al. [125] conduct schlieren imaging using a z-folded configuration to visualise blast wave propagation. A Shimadzu HPV-X2 camera captured the high-speed video at 500,000 fps. The urban model consisted of thin 3D-printed structures confined between transparent 6.35 mm-thick PMMA panels. The schlieren imaging was post-processed in order to automate feature tracking (e.g., edge detection) of shock fronts. The algorithms used are detailed in the previous work of Zheng et al. [126]. The processed schlieren photographs were compared against simulated frames at the same time after detonation. Remarkable similarities were seen between the sets of images, with the incident and primary reflections showing reasonably clearly in both sets. Here, schlieren imaging seems less effective at capturing more complex behaviours; this may be because the specific schlieren setup was not optimal to capture this detail, or perhaps this portrays a general limitation of schlieren imaging.

#### 4.1.3. Retroreflective Shadowgraphy

Hargather and Settles [127] explored improvements to retroreflective shadowgraph techniques. Retroreflective shadowgraphy requires three core elements: a light source, a screen and a camera. Note that Edgerton originally advanced this technique by modernising the work of Robert Hooke (1672) and applying the method to produce imaging of

gunshots and explosions [128,129]. The basic setup from Edgerton is shown in Figure 10. The light cast onto the screen refracts through disturbances in the air caused by an explosion, casting a shadow onto the back screen. This setup is simple, and many tolerances exist that achieve a good-quality image. A retroreflective screen is preferred over a simple white screen as the reflected light is largely directed back to the source, increasing the light intensity at the camera lens—essential for high-speed imaging. One factor that must be accounted for is the parallax, which will make shocks appear slightly smaller.

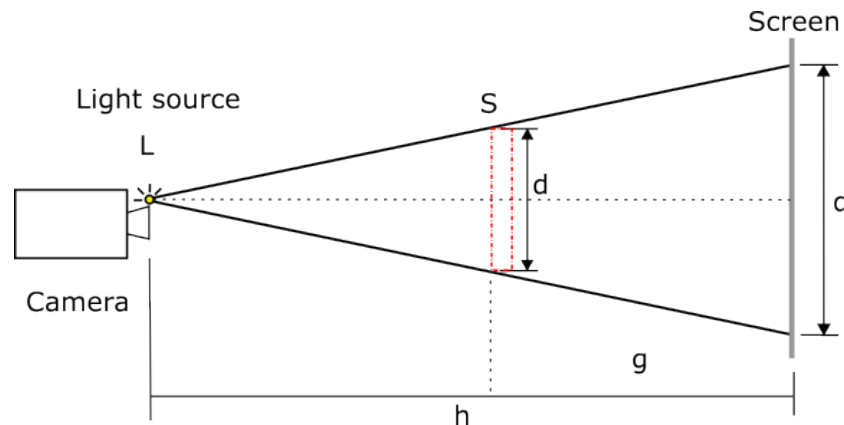


**Figure 10.** Basic retro-reflective shadowgraph set-up, adapted from Hargather and Settles [127].

Hargather and Settles [127] proposed a number of improvements to the retroreflective shadowgraphy technique. The principal improvement involves coinciding with the camera lens and the light source to eliminate double imaging and better show “*thin, sharp refractive disturbances*”. The most viable optical configuration utilises a rod mirror that can fit over a camera lens; a diagram is shown in Figure 11. The rod mirror setup was found to minimise light losses and removes the possibility of double imaging; thus, it was the preferred approach. The study showcases some experimental imaging captured using the rod mirror technique that reinforces the high-quality imaging possible from this approach.

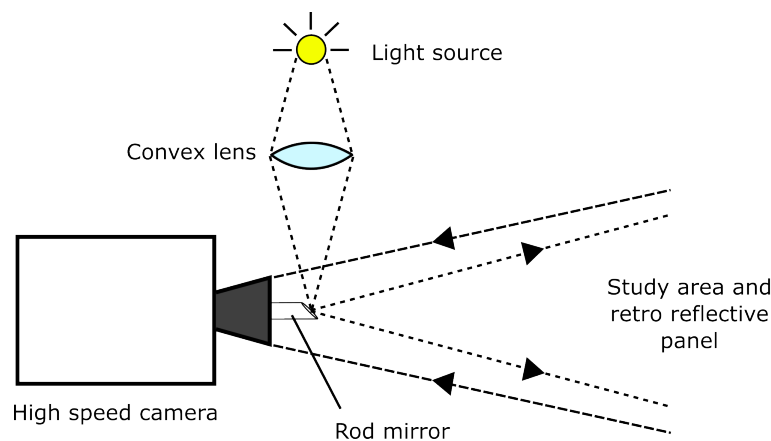


**Figure 11.** Diagram of the retroreflective shadowgraphy setup using a rod mirror, adapted from Hargather and Settles [127].

Gautier et al. [33] also utilised a variation of this imaging to capture shock wave interaction with finite obstacles. The “pure in-line shadowscopy” (PILS) method was formerly used by Slangen et al. [130]; it is well-equipped for ultra-high-speed imaging and shares many aspects with the previously discussed retroreflective shadowgraph technique. The optical configuration used is shown in Figure 12. Here, a transparent blast table is used to allow for a view of the retroreflective panel underneath. Some distance between the study area and the retroreflective panels is required to improve the optical sensitivity of the shadowscopy system. Generally, sensitivity is maximised when the distance between the

panel and the study area is 30–70% of the distance between the study area and the camera. A smaller distance allows for better-focused imaging, and a larger distance results in bolder shadows cast onto the screen.

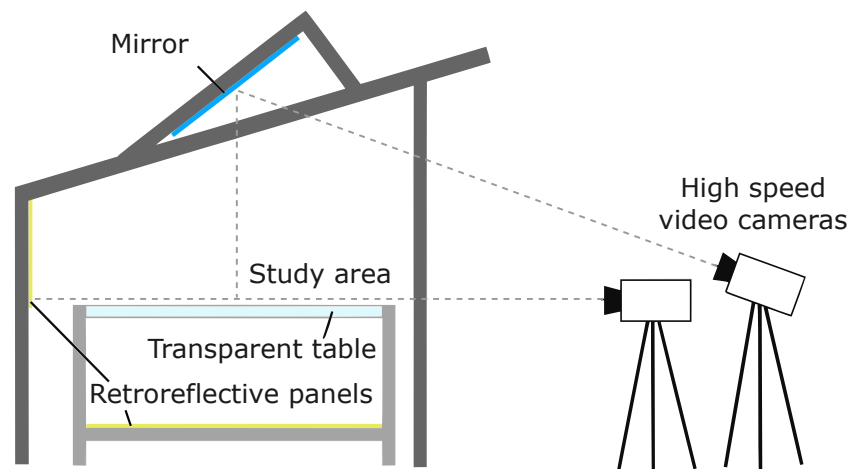


**Figure 12.** PILS imaging configuration to obtain a side view and plan view of the study area, adapted from Gautier et al. [33].

#### 4.2. Pressure Measurements

##### 4.2.1. Overview

Pressure is a key parameter regarding blasts, but it is difficult to measure accurately since direct measurement cannot, by definition, be non-intrusive. Therefore any measurement devices will themselves be subjected to the pressures they measure and the flow will be fundamentally altered. This makes it difficult to distinguish the source of variation in pressure data; what portion of variation (if any) can be attributed to originate from the pressure sensor, and what from the blast itself? If the sophistication of pressure measurement instrumentation can be improved, then the observed variance in a given dataset can be more confidently attributed to genuine physical processes of the explosion and blast propagation. A typical pressure sensor should be robust, have a small profile, a high natural frequency, optimal damping, and be insensitive to (electrical) noise. Attempting to improve one property can adversely impact another property, the effects of which are magnified at a very small scale.

##### 4.2.2. Optical Pressure Sensors

Watson et al. [131] explore the use of fibre-optic pressure sensors compared to electrical sensors. The experimental setup consisted of a  $2 \times 2$  m table where a hemispherical charge was placed in the centre. Two steel structures were placed at 0.654 m and 1.010 m away from the explosive. The furthest structure was instrumented with both pressure sensors, the closest only containing electrical sensors to ensure the optical sensors functioned within their maximum design range (up to 900 kPa).

Over 40 tests were conducted with varying explosive masses between 30–80 g. It is stated that “favourable performance of the optical sensors has been established against electrical sensors in a series of experimental tests measuring blast waves from small explosive charges”. The main reason for this was attributed to the optical sensors’ low susceptibility to acceleration, leading to less variation in overpressure readings. Figure 13 details the pressure–time measurements from the two types of sensors [131].

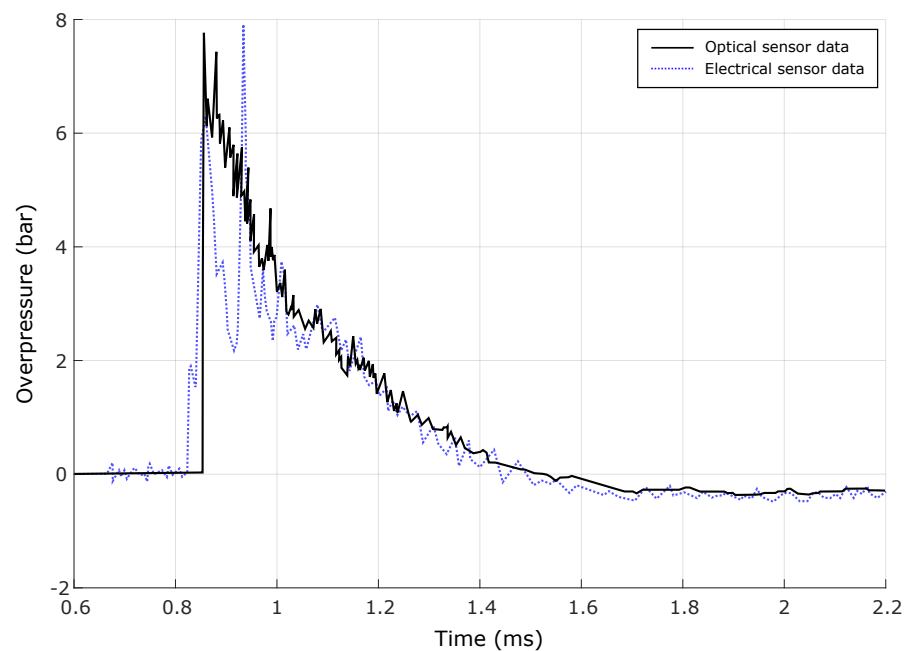


**Figure 13.** Measured reflected overpressures using electrical and optical sensors, adapted from [131].

An overview covering optical fibre technology conducted by Schenato [132] states that “single-point fibre optic sensor technologies have been proposed as solutions for pressure sensing for many years”. The conventional optical-fibre pressure sensors are Fiber Bragg Gratings and interferometric-based ones. Due to their reliability, multiple variations of pressure sensors of these types have been released as commercial products. Some advanced features include minimal invasiveness, refined measurement accuracy, immunity to electromagnetic interference and resistance to noise from acceleration.

#### 4.2.3. Piezoresistive/Piezoelectric Pressure Sensors

Piezoresistive-type pressure gauges (along with piezoelectric-type) are widely used for pressure and impulse data acquisition throughout experimental work within the blast engineering field [133,134]. Rigby et al. [135] use such instrumentation to study angle of incidence effects on positive and negative phase blast parameters in the far field. Four Kulite HKM piezoresistive pressure gauges were set flush against small steel plates, mounted within a larger concrete wall. Multiple combinations of charge mass (PE4) ranging between 180 g to 350 g, standoff distance and angle of incidence were tested. This included tests at an angle of incidence of  $0^\circ$ , which can otherwise be treated as standard normally reflected tests. Test data obtained from this angle of incidence were shown to be in very good agreement with semi-empirical values (e.g., ConWep). The normalised peak overpressure was seen to deviate by no more than 4–5%, similar to the confidence levels presented in Rigby et al. [13]. However, it was necessary to process the raw data using curve fitting techniques due to “the tendency for the signals to display some degree of electrical noise” and “sensor ringing”.

Such pressure gauges have been extensively proven for use in blast experimentation and can therefore be used to verify more speculative and novel diagnostic techniques such as pressure-sensitive paint [136,137].

#### 4.2.4. Fiber Bragg Grating Pressure Sensors

Hegde et al. [138] explore Fiber Bragg grating (FBG) sensors for space exploration applications. However, experiments were conducted with pressure ranges generally comparable to those from urban blast scenarios. A FBG sensor consists of an optical fibre section containing a repeating pattern of multiple reflection points. This pattern reflects certain wavelengths of incident light and allows all others to transmit through it. FBG sensors measure changes in Bragg wavelength due to an external stimulus, causing a strain that

alters the grating spacing. This change can be used to accurately measure pressure changes at high frequencies. Temperature compensation can be achieved by using an additional FBG sensor attached to a location insensitive to experimental inputs. Test data can then be calibrated using the control sensor data.

The pressure sensors were tested through shock tube experiments. A FBG sensor with a sampling rate of 2500 Hz was situated at the open end of the shock tube. The sensor was placed in a manner that would cause a tensile strain. This was achieved by placing the sensor within a housing parallel to a diaphragm, which would deflect outwards in the presence of a positive pressure differential. The sensitivity of the FBG sensor was determined beforehand via static pressure calibration and was found to have a value of 3.64 pm/bar. Two trials were conducted where the peak Bragg wavelength shift was found to be 68 pm and 99 pm, respectively. This corresponded to absolute pressure measurements of 19.59 bar and 27.19 bar, whereas the driver pressures were 18.5 bar and 19.9 bar. This is quoted as “*observed to be within an error of 1% of full scale (700 bar)*”.

#### 4.2.5. Extrinsic Fabry–Perot Interferometric Pressure Sensors

Ma et al. [139] propose and demonstrate the use of an extrinsic Fabry–Perot interferometric (EFPI) pressure sensor. The EFPI sensor measures changes in the silicon cavity length caused by a pressure differential between the internal and external pressures. The sensor has low intrusiveness, with face dimensions of 4.3 mm × 4.3 mm. The pressure sensor was tested experimentally, although the nature of the pressure application was static, so a direct comparison to other pressure sensors that are tested dynamically cannot yet be made. The pressure sensor underwent a calibration test where it was exposed to a gradual increase in pressure from 0 MPa to 1 MPa. The results showed a strong linear relationship between the cavity length and the applied pressure, achieving a regression coefficient of 0.99993. Additionally, the pressure resolution was 18.77 Pa from these results, less than 0.002% error at full scale. Clearly, further testing is required to determine how this particular pressure sensor would perform in dynamic pressure tests.

#### 4.2.6. Hybrid Pressure Sensor Usage

Clarke et al. [140] utilise a large-scale experimental set-up for measuring spatially and localised loading caused by the detonation of shallow-buried [141–143] and near-field free-air explosives [144]. They explore a range of instrumentation techniques, which are summarised in a tabulated format. The options include:

- Hopkinson pressure bars (HPBs);
- Stress gauges;
- Piezo electric/resistive pressure gauges;
- Impulse momentum traps;
- Load cells.

Clarke et al. [140] were interested in capturing peak overpressures whilst also aiming to measure “*long duration stagnation pressures*”. From their initial instrumentation considerations, it was apparent that a single pressure sensor type could not achieve the desired measurements suitably. Therefore, the decision was made to utilise multiple sensor types. Hopkinson [145] pressure bars (HPBs) were used to measure peak overpressures in conjunction with load cells for the longer-duration pressures.

The duration for which a HPB can record loading is determined by the time taken for an elastic stress pulse to reach the end of the bar and return to the location of the strain gauge. Consequently, the maximum measurable load duration is limited by the length. As used in experimental testing, HPBs with lengths of 3.25 m could measure for a load duration of 1.2 ms. The HPBs used could achieve an effective sampling rate of up to 250 kHz with a radius of 5 mm for the bars (selected to balance sampling rate and the need for a larger bar diameter to capture representative loading from discrete particle strikes). HPBs have been used successfully as dynamic force transducers [146–155]; however, the need for a considerable bar length limits the scenarios and positions where HPBs can be

utilised within experimental testing. More information on the use of HPBs for blast load characterisation is available in the review of Rigby et al. [156].

### 4.3. Small-Scale Blast Waves

#### 4.3.1. Gas Bubbles

Blanc et al. [157] experimentally and numerically explored the reflection of shock waves on complex buildings. The experiments were conducted at a scale of 1:60 atop an instrumented blast table. The shock waves were generated from detonating a hemispherical soap bubble containing a mixture of propane and oxygen. The gas mixture was ignited via the vaporisation of a small copper wire when a high voltage is passed through it. Gautier et al. [33] also used a similar approach for shock wave generation to conduct experimental work. This method of shock generation was shown to have good repeatability regarding measured overpressures and impulses for a single sensor located in front of the centre of detonation. Three tests were conducted, and it was seen that the discrepancies between overpressure test data were under 5%. This technique shows good promise, but the scope of this control-type test is limited, and the smallest possible scale for this type of detonation is not discussed.

#### 4.3.2. Exploding Wire

Dela Cueva et al. [125] created an experimental setup that enables a better understanding of the interaction between shock waves and structures. An exploding wire setup was used for the study. This method works by discharging a current from a large voltage through a spark gap. The current then travels through the experimental setup, reaching a test section consisting of a thin copper wire. The section of copper wire is rapidly heated and reaches a plasma state, which generates a shock wave upon expansion. The desired voltage output can be selected to explore a range of input parameters. The stated experimental turnout was said to be 100 s per test, so the system is suitable for rapid data collection.

#### 4.3.3. Pressurised Glass Spheres

Courtiaud et al. [158] conducted an experimental and numerical-based study to analyse the mixing within high-explosive fireballs. The bursting of pressurised glass spheres was used to mimic the flow caused by the detonation of an explosive mass. This method is referred to as the “compressed balloon method”, and the flow behaviour is representative of a spherical detonation. As no detonation occurred, there was no fireball, and the clarity of images taken in the blast’s early stages was improved significantly compared to imaging of conventional blasts.

The repeatability of the method used was not the main subject of the paper, so there is limited information regarding this. Numerical results showed some behavioural agreement with the experimental results, but a key difference was noted. The shock waves were seen to “follow a slower formation process in the experiments than in the simulation”. This was attributed to the glass fragments from the shattered glass spheres modifying the flow in the experiments.

#### 4.3.4. Pellets

Tamba et al. [159] generated blast waves through the detonation of 1 g pentaerythritol tetranitrate pellets to study additional protection methods of standard walls against blasts. The pellets were formed by glueing two 0.5 g pellets together and were initiated by an electrical detonator attached on top. The repeatability of this approach was not commented on within the paper directly; however, it was stated that tests without any obstacles were performed as a reference, but no further detail was given. Additionally, the pressure sensors of interest were only spaced apart at a maximum radial angle of 20 degrees, which limits the ability to investigate proof of uniformity in the shock wave. Using pre-made pellets may serve as a rapid method to conduct future experimental tests, but further testing on their suitability in terms of uniformity may be required.

#### 4.3.5. Laser-Induced Plasma

Bae et al. [160] utilised plasma induction via lasers for implementing calibration-free seedless velocimetry. The technical aspects and outcomes of the majority of this paper are beyond the scope of this literature review. However, the shock wave formation involved in the experimental work forms an area of interest. When a laser pulse of high intensity is focused at a singular point within a gas, the molecules in the “focal volume” will form an intense plasma, otherwise termed laser-induced plasma (LIP) [160,161]. Temperatures and pressures within the plasma are reported to reach over 20,000 °K and 540 kPa, respectively [162]. This causes the formation of a strong shock wave, although at an extremely small scale.

Laser-induced plasma could be a rapid shock wave generation method for minuscule-scaled blast experiments. Some initial challenges present themselves, including the non-uniformity of the shock wave and the scalability of this approach. At a time of 1000 ns, the approximate diameter of the shock wave in the  $x$  direction is 4.5 mm and in the  $y$  direction is 3.5 mm. Additionally, the 1000 ns shock image was the latest one captured; earlier images displayed even more non-uniformity. In regards to the scalability, it may be reasonable to assume that a higher-power laser would produce a more intense plasma or be able to induce plasma in a larger focal volume. These assumptions are speculative and require further investigation. Laser-induced plasma may also serve as a detonation method to initiate sub-gram explosives as a substitute for conventional detonators, which can significantly alter blast propagation for small explosive masses.

#### 4.3.6. Detonation Transmission Tubing

Isaac Samuelraj et al. [163] explored the use of detonation transmission tubing (DTT) to study and visualise micro-blast waves. The tubing used, termed a Nonel tube, consists of a small-diameter tube, which is internally coated with a thin layer of explosive compound. This equates to an explosive loading of roughly 18 mg per meter of tube length. To initiate detonation, a spark is generated at the distal end of the tube. A schlieren setup was used to capture high-speed video of the tests. CFD was also used in a comparative basis. Both the high-speed video and the CFD displayed a visually uniform circular blast front from the detonation of the DTT. However, the pressure data suggested a non-uniform strength of the blast wave was prevalent. The blast front that continued along the same trajectory as the axis of the tubing displayed significantly higher pressures than aspects of the blast wave directed radially to the tube (similar to findings from long aspect-ratio charges [20]). This effect was attributed to the “*directed momentum of the jet of combustion products along the tube axis*” [163]. If this non-uniformity can be accounted for, then DTT may serve as a viable approach to shock generation for small-scale blast experiments.

## 5. Summary and Conclusions

### 5.1. Current Knowledge

This review has explored a comprehensive range of literature to supplement the reader with a variety of knowledge relevant to urban blasts. Some well-understood and common behaviours of urban blast events have been discussed, as well as some contradictions. One particular contradiction relates to the findings within Ripley et al. [47] and Donahue et al. [51], where it is shown that the degree of confinement has a reasonable positive correlation with the average blast load. The degree of confinement can be considered as a metric of “how confined” a blast would be if it were to be detonated in a certain volume and increases as objects are placed in it. These findings could be interpreted to show the opposite of what Fouchier et al. [42] found, where the scaled impulse decreases slightly within a confining array. However, it is difficult to directly compare the findings as a common measure for the degree of confinement is not used throughout. A meta-analysis that utilises the degree of confinement metric and applies it to urban-style blast experiments is recommended to allow for an improved comparison basis.

In addition to this, Fouchier et al. [42] found that once a blast exits the confinement of an array, it experiences a sharp drop (roughly 80%) in impulse and overpressure compared to that of a free-field scenario. This effect is not seen in Smith et al. [37], where the scaled impulse across a wall beyond the array experiences a minor decrease (roughly 13%) compared to a free-field scenario. A potential aim for future work would be to provide further knowledge of these findings to explain the differences seen from these results through experimental work.

### 5.2. Numerical Methods

Numerical simulations have been shown to offer accurate results regarding the analysis of blasts, with CFD- and neural-network-based approaches being the most sophisticated. Compared to simplified empirical methods, the utilisation of numerical simulations provides a significant improvement to blast parameter predictions. CFD simulations can reasonably accurately capture complex flow-field behaviours in their current state. However, these models may be subject to further refinement to improve their accuracy and are computationally expensive to run. It is not universally agreed upon what fidelity, features and inputs are required in these simulations to ensure satisfactory agreement with experimental measurements. Indeed, the lack of available high-quality experimental data—with comparable sophistication and detail to numerical modelling approaches—is currently hampering these efforts.

Further experimental-based work should attempt to supplement the knowledge basis regarding numerical simulations by defining reasonable standards that future models should try to achieve. For example, it may be possible to determine the sensitivity of more minor structural or geometric features that are usually not numerically modelled. These are typically assumed to offer little change in the results compared to the additional computational resources required; however, this assumption is made with little justification [99] and the influence of such features on the solution remains unknown. It is also clearly shown that numerical modelling can be utilised to provide verification at multiple stages of experimental work, further acting as a means to provide additional data in certain studies. Understanding the physical behaviours from experimental work can assist in validating numerical models; an example of this is given by the experimental work of Gajewski and Sielicki [164] being used to validate related modelling work conducted by Denny et al. [165]. In this regard, the authors wish to highlight the importance of experimentalists publishing their collected data in full and in an accessible format, in order to facilitate rigorous and detailed validation of future modelling efforts.

### 5.3. Experimental Possibilities

A sophisticated range of instrumentation and imaging techniques have been explored, the majority of which could be feasible for use within experimental work. Retro-reflective shadowgraphy has been showcased as an effective means of capturing high-quality blast images [127]. It is likely to be pursued as the imaging technique used for most future experimental work, and there exists some potential to substitute high-cost equipment for affordable counterparts.

Regarding pressure sensor instrumentation, it is difficult to identify a well-agreed-upon “best” solution. Pressure remains a difficult metric to measure accurately and smoothly due to the intrusive nature of instrumentation; for example, the D1 pressure data in Table 2 varies by over 50%, among other smaller variations [107]. Whilst there is no consensus on the optimal pressure sensor type, configuration, design, etc., this consideration will likely become more important as experimental complexity and fidelity increase and the need to provide definitive, accurate, and repeatable experimental data for model validation becomes more pressing. Currently, it would be reasonable to state that the pressure sensor instrumentation used in any experimental work should be chosen based on the use case and availability. However, it is difficult to justify an in-depth, custom study to find the best instrumentation for a specific experimental package when a variation of 5% or 15%

could both be considered acceptable experimental variance unless time and cost restraints are relaxed. Clearly, further work is required to determine the exact sources of variation in blast load measurements, and to quantify their magnitude and statistical properties, in order to more definitively bound experimental error.

#### 5.4. Outlook

This review has extensively explored the knowledge base of urban blasts, highlighting common knowledge and areas of ignorance regarding blast wave behaviour, measurement, and prediction. There is a clear requirement for tools and metrics that can better predict urban blast parameters within city-like geometries (such as that used by Donahue et al. [51]) that do not require high computational demand in order to enable rapid predictions for quick response times. Clearly, improved methodologies such as this, and an improved understanding of blast loading in cityscapes, will lead to significant advancements in risk-based studies for the resilience of urban areas to terrorist events [166,167]. A current lack of a sophisticated experimental framework severely limits the ability to progress this understanding.

CFD simulations are generally capable of replicating experimental data with good accuracy and can provide a verification approach to novel experimental work. However, despite ongoing attempts to expedite numerical analyses [168], they generally lack the necessary short computation times required for decision-making, emergency response, or even parameter-rich, risk-based studies. Neural networks have been shown to significantly improve upon the issue of computation time compared to CFD methods, and their utilisation will likely spread throughout the field as a preferred numerical-based approach in the coming years as training datasets become more thorough and data-rich. This leads to a requirement for experimental approaches that are capable of producing precise and accurate data rapidly; the same can be said for the formation of predictive tools and metrics.

Numerical modelling capabilities have outpaced the ability to rigorously validate them using experimental techniques, and current modelling advancements are being made in the absence of any real knowledge of their accuracy or sensitivities. Indeed, some numerical models have been validated against other numerical models, such is the gulf between numerical and physical capabilities. Naturally, there is a clear requirement for significant advances in experimental approaches and instrumentation to improve the accuracy and precision of acquired data. Experimental cost and turnover can be improved by conducting experimental tests at the smallest scale feasible. With that, it is recommended that working towards a standard of utilising sophisticated, high-fidelity, smaller-scale experimental work within the field should become a key focus to meet a potential surge in demand for large, reliable datasets.

**Author Contributions:** Original draft preparation, A.R.; writing and editing, A.R., S.R.; review, S.R., S.C., S.F.; supervision, S.R., S.C.; funding acquisition, S.R., S.C.; industry contact, S.F. All authors have read and agreed to the published version of the manuscript.

**Funding:** This review was performed as part of an iCASE studentship funded by EPSRC and the Atomic Weapons Establishment, grant number 40019823.

**Institutional Review Board Statement:** Not applicable.

**Informed Consent Statement:** Not applicable.

**Data Availability Statement:** No new data was generated for this review.

**Conflicts of Interest:** The authors declare that there are no conflicts of interest.

## References

1. Ritchie, H.; Roser, M. Plastic Pollution. 2018. Available online: <https://ourworldindata.org/plastic-pollution> (accessed on 11 November 2022).
2. Dusenberry, D. *Handbook for Blast-Resistant Design of Buildings*; John Wiley & Sons, Hoboken, NJ, USA, 2010.
3. Norville, H.S.; Harvill, N.; Conrath, E.J.; Shariat, S.; Mallonee, S. Glass-related injuries in Oklahoma City bombing. *J. Perform. Constr. Facil.* **1999**, *13*, 50–56. [[CrossRef](#)]

4. Rigby, S.E.; Lodge, T.; Alotaibi, S.; Barr, A.; Clarke, S.; Langdon, G.; Tyas, A. Preliminary yield estimation of the 2020 Beirut explosion using video footage from social media. *Shock Waves* **2020**, *30*, 671–675. [[CrossRef](#)]
5. Rufolo, P.; Muraro, D.; Lorini, V. *Social Media Image Analysis in the Immediate Aftermath of the 2020 Beirut Blast*; Technical Report JRC124081; Joint Research Centre, Publications Office of the European Union: Luxembourg, 2021.
6. Halswijk, W. BeamBlast: Blast path-finding algorithms. In Proceedings of the 16th ISIEMS International Symposium for the Interaction of the Effects of Munitions with Structures, Destin, FL, USA, 9–13 November 2015.
7. Adhikary, S.; Dutta, S. Blast resistance and mitigation strategies of structures: Present status and future trends. *Proc. Inst. Civ. Eng. Struct. Build.* **2019**, *172*, 249–266. [[CrossRef](#)]
8. Cormie, D.; Mays, G.; Smith, P. *Blast Effects on Buildings*, 2nd ed.; Thomas Telford: London, UK, 2009.
9. Duncan-Miller, G. Urban Blast Waves: A Semi-Analytic Solution for Intense Explosions with Rigid Wall Reflections. Ph.D. Thesis, Department of Mathematics, New Mexico Institute of Mining and Technology, Socorro, NM, USA, 2016.
10. Larcher, M.; Casadeia, F. Explosions in complex geometries—A comparison of several approaches. *Int. J. Prot. Struct.* **2010**, *1*, 169–196. [[CrossRef](#)]
11. Stirling, C.; Misselbrook, N.; Nikodym, L.; Mould, J.; Wesevic, J. The importance of considering realistic blast waveforms and corresponding methods of assessing structural damage when conducting quantitative risk assessments. In Proceedings of the IChemE Hazards 27, Birmingham, UK, 10–12 May 2017.
12. Rigby, S.E.; Tyas, A.; Bennett, T.; Clarke, S.D.; Fay, S.D. The negative phase of the blast load. *Int. J. Prot. Struct.* **2014**, *5*, 1–20. [[CrossRef](#)]
13. Rigby, S.; Tyas, A.; Fay, S.; Clarke, S.; Warren, J. Validation of semi-empirical blast pressure predictions for far-field explosions—is there inherent variability in blast wave parameters? In Proceedings of the 6th International Conference on Protection of Structures against Hazards, Tianjin, China, 16–17 October 2014.
14. Rigby, S.; Knighton, R.; Clarke, S.; Tyas, A. Reflected near-field blast pressure measurements using high speed video. *Exp. Mech.* **2020**, *60*, 875–888. [[CrossRef](#)]
15. Hopkinson, B. *British Ordnance Board Minutes 13565*; Public Records Office: London, UK, 1915; Volume 187.
16. Cranz, C. *Lehrbuch der Basllistik*; Springer: Berlin/Heidelberg, Germany, 1926.
17. Rigby, S.E.; Tyas, A.; Curry, R.J.; Langdon, G.S. Experimental Measurement of Specific Impulse Distribution and Transient Deformation of Plates Subjected to Near-Field Explosive Blasts. *Exp. Mech.* **2019**, *59*, 163–178. [[CrossRef](#)]
18. Rigby, S.E.; Akintaro, O.I.; Fuller, B.J.; Tyas, A.; Curry, R.J.; Langdon, G.S.; Pope, D.J. Predicting the response of plates subjected to near-field explosions using an energy equivalent impulse. *Int. J. Impact Eng.* **2019**, *128*, 24–36. [[CrossRef](#)]
19. Rigby, S.; Osborne, C.; Langdon, G.; Cooke, S.; Pope, D. Spherical equivalence of cylindrical explosives: Effect of charge shape on deflection of blast-loaded plates. *Int. J. Impact Eng.* **2021**, *155*, 103892. [[CrossRef](#)]
20. Langran-Wheeler, C.; Rigby, S.E.; Clarke, S.D.; Tyas, A.; Stephens, C.; Walker, R. Near-field spatial and temporal blast pressure distributions from non-spherical charges: Horizontally-aligned cylinders. *Int. J. Prot. Struct.* **2021**, *12*, 492–516. [[CrossRef](#)]
21. Tyas, A.; Reay, J.J.; Fay, S.D.; Clarke, S.D.; Rigby, S.E.; Warren, J.A.; Pope, D.J. Experimental studies of the effect of rapid afterburn on shock development of near-field explosions. *Int. J. Prot. Struct.* **2016**, *7*, 456–465. [[CrossRef](#)]
22. Rigby, S.; Sielicki, P. An investigation of TNT equivalence of hemispherical PE4 charges. *Eng. Trans.* **2014**, *62*, 423–435.
23. Bogosian, D.; Yokota, M.; Rigby, S. TNT equivalence of C-4 and PE4: A review of traditional sources and recent data. In Proceedings of the 24th International Symposium on Military Aspects of Blast and Shock (MABS24), Halifax, NS, Canada, 19–23 September 2016.
24. Grisaro, H.; Edri, I.; Rigby, S. TNT equivalency analysis of specific impulse distribution from close-in detonations. *Int. J. Prot. Struct.* **2021**, *12*, 315–330. [[CrossRef](#)]
25. Farrimond, D.G.; Woolford, S.; Tyas, A.; Rigby, S.E.; Clarke, S.D.; Barr, A.; Whittaker, M.; Pope, D.J. Far-field positive phase blast parameter characterisation of RDX and PETN based explosives. *Int. J. Prot. Struct.* **2023**, *ahead of print*.
26. Smith, P.; Mays, G.; Rose, T.; Teo, K.; Roberts, B. Small scale models of complex geometry for blast overpressure assessment. *Int. J. Impact Eng.* **1992**, *12*, 345–360. [[CrossRef](#)]
27. Johnson, E.M.; Grahl, N.; Langenderfer, M.J.; Doucet, D.P.; Schott, J.; Williams, K.; Rutter, B.; Johnson, C. An experimental and simulated investigation into the validity of unrestricted blast wave scaling models when applied to transonic flow in complex tunnel environments. *Int. J. Prot. Struct.* **2022**, *ahead of print*.
28. Xiao, W.; Andrae, M.; Gebbeken, N. Air blast TNT equivalence concept for blast-resistant design. *Int. J. Mech. Sci.* **2020**, *185*, 105871. [[CrossRef](#)]
29. Hyde, D.W. *Microcomputer Programs CONWEP and FUNPRO, Applications of TM 5-855-1, 'Fundamentals of Protective Design for Conventional Weapons (User's Guide)*; Technical Report; Army Engineer Waterways Experiment Station Vicksburg MS Structures Lab.: Vicksburg, MS, USA, 1988.
30. Britt, J.R.; Lumsden, M.G. *Internal Blast and Thermal Environment from Internal and External Explosions: A User's Guide for the BLAST-X Code, Version 3.0*; Technical Report SAIC 405-94-2; Science Applications International Corporation: St. Joseph, LA, USA, 1994.
31. Angelides, S.; Burgan, B.; Kyprianou, C.; Rigby, S.; Tyas, A. EMBlast: A software for rapidly and accurately calculating blast loads on structures. In Proceedings of the 97th Comité International Des Construction Industrielles (CICIND) Conference, Paphos, Cyprus, 19–21 October 2022.

32. Smith, P.D.; Rose, T.A. Blast wave propagation in city streets—An overview. *Prog. Struct. Eng. Mater.* **2006**, *8*, 16–28. [[CrossRef](#)]
33. Gautier, A.; Sochet, I.; Courtaud, S. Analysis of shock wave interaction with an obstacle by coupling pressure measurements and visualization. *Sensors* **2022**, *22*, 3325. [[CrossRef](#)]
34. Gautier, A.; Sochet, I.; Lapebie, E.; Boubrit, A. Shock Wave Propagation in an Obstructed Area. *Wit Trans. Built Environ.* **2020**, *198*, 15–27.
35. Gautier, A.; Sochet, I.; Lapebie, E. Analysis of 3D interaction of a blast wave with a finite wall. *Shock Waves* **2022**, *32*, 273–282. [[CrossRef](#)]
36. Hajek, R.; Foglar, M.; Fladr, J. Influence of barrier material and barrier shape on blast wave mitigation. *Constr. Build. Mater.* **2016**, *120*, 54–64. [[CrossRef](#)]
37. Smith, P.; Rose, T.; Ng, S. The influence of areal density on the shielding and channelling of blast by buildings. In Proceedings of the 18th International Symposium on Military Aspect of Blast and Shock (MABS18), Bad Reichenhall, Germany, 27 September–1 October, 2004.
38. Rose, T.A. *Air3d User's Guide*; Cranfield University, Royal Military College of Science: Shrivenham, UK, 2002.
39. Boeing, G. Urban spatial order: Street network orientation, configuration, and entropy. *Appl. Netw. Sci.* **2019**, *4*, 67. [[CrossRef](#)]
40. Smith, P.; Rose, T.; Green, J. The effect of arrays of suburban buildings in providing shielding from blast. In Proceedings of the 11th International Symposium on Interaction of the Effects of Munitions with Structures, Mannheim, Germany, 5–9 May 2003.
41. Gan, K.; Brewer, T.; Pope, D.; Rigby, S. Probabilistic analysis of blast–obstacle interaction in a crowded internal environment. *Probabilistic Eng. Mech.* **2022**, *68*, 103227. [[CrossRef](#)]
42. Fouchier, C.; Laboureur, D.; Youinou, L.; Lapebie, E.; Buchlin, J. Experimental investigation of blast wave propagation in an urban environment. *J. Loss Prev. Process Ind.* **2017**, *49*, 248–265. [[CrossRef](#)]
43. Smith, P.; Whalen, G.; Feng, L.; Rose, T. Blast loading on buildings from explosions in City Streets. *Proc. Inst. Civ. Eng. Struct. Build.* **2001**, *146*, 47–55. [[CrossRef](#)]
44. Kinney, G.F.; Graham, K.J. Internal blast. *Explosive Shocks in Air*; Springer: Berlin/Heidelberg, Germany, 1985; pp. 137–160.
45. France groupe d'étude des Modes Operatoires (GEMO). *Determination Desequivalents tnt par Effetde Souffle des Explosifs*; GEMO: Lyon, France, 2013.
46. Rose, T.; Smith, P. Influence of the principal geometrical parameters of straight city streets on positive and negative phase blast wave impulses. *Int. J. Impact Eng.* **2002**, *27*, 359–376. [[CrossRef](#)]
47. Ripley, R.; Cloney, C.; Donahue, L.; Zhang, F. Extended near-field regime in urban confinement. In Proceedings of the 22nd International Symposium on Military Aspects of Blast and Shock, Bourges, France, 4 November 2012.
48. Donahue, L.; Zhang, F.; Ripley, R. Numerical models for afterburning of TNT detonation products in air. *Shock Waves* **2013**, *23*, 559–573. [[CrossRef](#)]
49. Anthistle, T.; Fletcher, D.; Tyas, A. Characterisation of blast loading in complex, confined geometries using quarter symmetry experimental methods. *Shock Waves* **2016**, *26*, 749–757. [[CrossRef](#)]
50. Sochet, I.; Gault, K.; Hakenholz, L. Propagation of shock waves in two rooms communicating through an opening. In *Direct Numerical Simulations—An Introduction and Applications*; IntechOpen: London, UK, 2019.
51. Donahue, L.; Ripley, R.; Zhang, F. Validation of the correlation between urban blast confinement and structural load. In Proceedings of the 24th International Symposium on Military Aspects of Blast and Shock (MABS24), Halifax, NS, Canada, 19–23 September 2016.
52. Smith, P.; Rose, T.; Krahe, S.; Franks, M. Façade failure effects on blast propagation along city streets. *Proc. Inst. Civ.-Eng.-Struct. Build.* **2003**, *156*, 359–365. [[CrossRef](#)]
53. Dib, N.; Zéhil, G.P.; Rigby, S. On the blast-wave shielding effect of porous buildings. *J. Fluids Struct.* **2022**, *115*, 103787. [[CrossRef](#)]
54. Dewey, J.; McMillin, D.; Classen, D. Photogrammetry of spherical shocks reflected from real and ideal surfaces. *J. Fluid Mech.* **1977**, *81*, 701–717. [[CrossRef](#)]
55. Nguyen-Dinh, M.; Lardjane, N.; Duchenne, C.; Gainville, O. Direct simulations of outdoor blast wave propagation from source to receiver. *Shock Waves* **2017**, *27*, 593–614. [[CrossRef](#)]
56. Pasman, H.; Fouchier, C.; Park, S.; Quddus, N.; Laboureur, D. Beirut ammonium nitrate explosion: Are not we really learning anything? *Process Saf. Prog.* **2020**, *39*, e12203. [[CrossRef](#)]
57. ElGharbawi, T.; Zarzoura, F. Damage detection using SAR coherence statistical analysis, application to Beirut, Lebanon. *ISPRS J. Photogramm. Remote Sens.* **2021**, *173*, 1–9. [[CrossRef](#)]
58. Agapiou, A. Damage Proxy Map of the Beirut Explosion on 4th of August 2020 as Observed from the Copernicus Sensors. *Sensors* **2020**, *20*, 6382. [[CrossRef](#)] [[PubMed](#)]
59. Kingery, C.; Bulmash, G. *Airblast Parameters from TNT Spherical Air Burst and Hemispherical Surface Burst*; Technical Report ARBRL-TR-02555. U.S Army BRL, Aberdeen Proving Ground: Harford County, MD, USA, 1984.
60. Stennett, C.; Gault, S.; Akhavan, J. An estimate of the TNT-equivalent net explosive quantity (NEQ) of the Beirut Port explosion using publicly-available tools and data. *Propellants Explos. Pyrotech.* **2020**, *45*, 1675–1679. [[CrossRef](#)]
61. Aouad, C.; Chemissany, W.; Mazzali, P.; Temsah, Y.; Jahami, A. Beirut explosion: TNT equivalence from the fireball evolution in the first 170 milliseconds. *Shock Waves* **2021**, *31*, 813–827. [[CrossRef](#)]
62. Díaz, J. Explosion analysis from images: Trinity and Beirut. *Eur. J. Phys.* **2021**, *42*, 035803. [[CrossRef](#)]
63. Díaz, J.; Rigby, S. Blast wave kinematics: Theory, experiments, and applications. *Shock Waves* **2022**, *32*, 405–415. [[CrossRef](#)]

64. Locking, P. The trouble with TNT equivalence. In Proceedings of the 26th International Symposium on Ballistics, Miami, FL, USA, 12–16 September 2011.
65. Sivaraman, S.; Varadharajan, S. Investigative consequence analysis: A case study research of beirut explosion accident. *J. Loss Prev. Process Ind.* **2021**, *69*, 104387. [[CrossRef](#)]
66. Pilger, C.; Gaebler, P.; Hupe, P.; Kalia, A.C.; Schneider, F.M.; Steinberg, A.; Sudhaus, H.; Ceranna, L. Yield estimation of the 2020 Beirut explosion using open access waveform and remote sensing data. *Sci. Rep.* **2021**, *11*, 14144. [[CrossRef](#)]
67. Ismail, S.; Raphael, W.; Durrand, E. Case study of the Beirut port explosion using 3D laser scan and nonlinear finite element model. *Res. Eng. Struct. Mater.* **2021**, *7*, 551–577. [[CrossRef](#)]
68. Ismail, S.A.; Raphael, W.; Durand, E.; Kaddah, F.; Geara, F. Analysis of the structural response of Beirut port concrete silos under blast loading. *Arch. Civ. Eng.* **2021**, *67*, 619–638.
69. Temsah, Y.; Jahami, A.; Aouad, C. Silos structural response to blast loading. *Eng. Struct.* **2021**, *243*, 112671. [[CrossRef](#)]
70. Yu, G.D.; Wang, Y.; Zheng, L.; Huang, J.; Li, J.L.; Gong, L.Z.; Chen, R.; Li, W.; Huang, J.; Duh, Y.S. Comprehensive study on the catastrophic explosion of ammonium nitrate stored in the warehouse of Beirut port. *Process Saf. Environ. Prot.* **2021**, *152*, 201–219. [[CrossRef](#)]
71. Goldstein, P. Reconciling conflicting estimates of the Beirut explosion yield and mushroom cloud height: Effects of an aqueous near source environment. *Countering Wmd J.* **2021**, *22*, 121–137.
72. Clough, L.G.; Clublely, S.K. Steel column response to thermal and long duration blast loads inside an air blast tunnel. *Struct. Infrastruct. Eng.* **2019**, *15*, 1510–1528. [[CrossRef](#)]
73. Denny, J.W.; Clublely, S.K. Long-duration blast loading & response of steel column sections at different angles of incidence. *Eng. Struct.* **2019**, *178*, 331–342.
74. Cannon, L.; Clublely, S.K. Structural response of simple partially-clad steel frames to long-duration blast loading. *Structures* **2021**, *32*, 1260–1270. [[CrossRef](#)]
75. Clublely, S.K. Non-linear long duration blast loading of cylindrical shell structures. *Eng. Struct.* **2014**, *59*, 113–126. [[CrossRef](#)]
76. Jiang, Y.; Zhang, B.; Wang, L.; Wei, J.; Wang, W. Dynamic response of polyurea coated thin steel storage tank to long duration blast loadings. *Thin-Walled Struct.* **2021**, *163*, 107747. [[CrossRef](#)]
77. Børvik, T.; Hanssen, A.; Langseth, M.; Olovsson, L. Response of structures to planar blast loads – A finite element engineering approach. *Comput. Struct.* **2009**, *87*, 507–520. [[CrossRef](#)]
78. Yang, S.; Liu, Z.; Wang, S.; Zhong, W.; Zhang, R.; Yao, X. Dynamic response and failure analysis for urban bridges under far-field blast loads. *Eng. Struct.* **2023**, *285*, 116043. [[CrossRef](#)]
79. Denny, J.W.; Clublely, S.K. Evaluating long-duration blast loads on steel columns using computational fluid dynamics. *Struct. Infrastruct. Eng.* **2019**, *15*, 1419–1435. [[CrossRef](#)]
80. Cannon, L.; Denny, J.; Clublely, S. Eulerian solver sensitivity for computing long-duration blast drag loading on columns. *Proc. Inst. Civ.-Eng.-Eng. Comput. Mech.* **2022**, *175*, 1–13. [[CrossRef](#)]
81. Warnstedt, P.; Gebbeken, N. Innovative protection of urban areas—Experimental research on the blast mitigating potential of hedges. *Landsc. Urban Plan.* **2020**, *202*, 103876. [[CrossRef](#)]
82. Alshammari, O.G.; Isaac, O.S.; Clarke, S.D.; Rigby, S.E. Mitigation of blast loading through blast–obstacle interaction. *Int. J. Prot. Struct.* **2022**, *ahead of print*.
83. Isaac, O.S.; Alshammari, O.G.; Clarke, S.D.; Rigby, S.E. Experimental investigation of blast mitigation of pre-fractal obstacles. *Int. J. Prot. Struct.* **2022**, *ahead of print*.
84. Isaac, O.S.; Alshammari, O.G.; Pickering, E.G.; Clarke, S.D.; Rigby, S.E. Blast wave interaction with structures—An overview. *Int. J. Prot. Struct.* **2022**, *ahead of print*.
85. Century-Dynamics. *AUTODYN Users Manual; Version 4.3*; Century-Dynamics: Concord, CA, USA, 2003.
86. Armstrong, B.J.; Rickman, D.D.; Baylot, J.T.; Bevins, T.L. Code validation studies for blast in urban terrain. In Proceedings of 2002 HPC User’s Group Conference, Austin, TX, USA, 10–14 June 2002.
87. Remennikov, A.; Rose, T. Modelling blast loads on buildings in complex city geometries. *Comput. Struct.* **2005**, *83*, 2197–2205. [[CrossRef](#)]
88. Johansson, M.; Larsen, O.; Laine, L. Explosion at an intersection in an Urban Environment—Experiments and analyses. In Proceedings of the 78th Shock and Vibration Symposium, Philadelphia, PA, USA, 4–8 November 2007.
89. Hank, S.; Saurel, R.; Le Métayer, O.; Lapébie, E. Modeling blast waves, gas and particles dispersion in urban and hilly ground areas. *J. Hazard. Mater.* **2014**, *280*, 436–449. [[CrossRef](#)] [[PubMed](#)]
90. Codina, R.H.; Ambrosini, D.; de Borbón, F. Numerical study of confined explosions in urban environments. *Int. J. Prot. Struct.* **2013**, *4*, 591–617. [[CrossRef](#)]
91. Drazin, W. Blast Propagation and Damage in Urban Topographies. Ph.D. Thesis, The Laboratory for Scientific Computing, Cavendish Laboratory, University of Cambridge, Cambridge, UK, 2017.
92. Mohr, L.; Benauer, R.; Leitl, P.; Fraundorfer, F. Damage estimation of explosions in urban environments by simulation. In Proceedings of the International Archives of the Photogrammetry, Remote Sensing and Spatial Information Sciences—ISPRS Archives Volume XLII-3/W8. Gi4DM 2019—GeoInformation for Disaster Management, Prague, Czech Republic, 3–6 September 2019; Volume 42, pp. 253–260.

93. Chi, M.; Jiang, H.; Lan, X.; Xu, T.; Jiang, Y. Study on Overpressure Propagation Law of Vapor Cloud Explosion under Different Building Layouts. *ACS Omega* **2021**, *6*, 34003–34020. [[CrossRef](#)] [[PubMed](#)]
94. Luccioni, B.; Ambrosini, R.; Danesi, R. Analysing explosive damage in an urban environment. *Proc. Inst. Civ. Eng. Struct. Build.* **2005**, *158*, 1–12. [[CrossRef](#)]
95. Ambrosini, D.; Luccioni, B.; Jacinto, A.; Danesi, R. Location and mass of explosive from structural damage. *Eng. Struct.* **2005**, *27*, 167–176. [[CrossRef](#)]
96. Christensen, S.O.; Hjort, Ø.J.S. Back Calculation of the Oslo Bombing on July 22nd, Using Window Breakage. In Proceedings of the 22nd International Symposium on Military Aspects of Blast and Shock, Bourges, France, 4 November 2012.
97. Marks, N.; Stewart, M.; Netherton, M.; Stirling, C. Airblast variability and fatality risks from a VBIED in a complex urban environment. *Reliab. Eng. Syst. Saf.* **2021**, *209*, 107459. [[CrossRef](#)]
98. Alterman, D.; Stewart, M.; Netherton, M. Probabilistic assessment of airblast variability and fatality risk estimation for explosive blasts in confined building spaces. *Int. J. Prot. Struct.* **2019**, *10*, 306–329. [[CrossRef](#)]
99. Valsamos, G.; Larcher, M.; Casadei, F. Beirut explosion 2020: A case study for a large-scale urban blast simulation. *Saf. Sci.* **2021**, *137*, 105190. [[CrossRef](#)]
100. Willenborg, B. *Simulation of Explosions in Urban Space and Result Analysis Based on CityGML City Models and a Cloud Based 3D Web Client*; Technical University Munich Chair of Geoinformatics: Munich, Germany, 2015
101. Sklavounos, S.; Rigas, F. Computer simulation of shock waves transmission in obstructed terrains. *J. Loss Prev. Process Ind.* **2004**, *17*, 407–417. [[CrossRef](#)]
102. Cullis, I.G.; Nikiforakis, N.; Frankl, P.; Blakely, P.; Bennett, P.; Greenwood, P. Simulating geometrically complex blast scenarios. *Def. Technol.* **2016**, *12*, 134–146. [[CrossRef](#)]
103. Brittle, M. Blast Propagation in a Geometrically Complex Environment. Ph.D. Thesis, Cranfield University, Cranfield, UK, 2004.
104. Brewer, T.; Vonk, P.; Heylmun, J. Blastfoam: A free and open-source CFD airblast code for simulating high-explosive detonation. *Explos. Eng.* **2020**, 27–31.
105. Brewer, T.; Vonk, P.; Heylmun, J. *Validation of the Blastfoam Airblast Solver*; Technical Report; Synthetik Applied Technologies: Austin, TX, USA, 2020; pp. 18–45.
106. Dörr, A.; Gürke, G.; Brugger, W. Validation Experiments for Blast Solver. In *Fraunhofer EMI Report*; Fraunhofer EMI: Freiburg im Breisgau, Germany, 2007
107. Lee, S.; Vlahopoulos, N.; Mohammad, S. Development of a Regression Model for Blast Pressure Prediction in Urban Street Configurations. In Proceedings of the 16th International LS-DYNA User Conference, Virtual Event, 10–11 June 2020.
108. Rose, T.A. An Approach to the Evaluation of Blast Loads on Finite and Semi-Infinite Structures. Ph.D. Thesis, Cranfield University, Cranfield, UK, 2010.
109. Remennikov, A.; Mendis, P. Prediction of airblast loads in complex environments using Artificial Neural Networks. *Wit Trans. Built Environ. Struct. Under Shock Impact IX Lisbon Port.* **2006**, *87*, 269–278.
110. Dennis, A.; Pannell, J.; Smyl, D.; Rigby, S. Prediction of blast loading in an internal environment using Artificial Neural Networks. *Int. J. Prot. Struct.* **2020**, *12*, 287–314. [[CrossRef](#)]
111. Ruscade, G.; Sochet, I.; Hakenholz, L.; Djafer, K. Shock Wave Propagation in a Double Room. *Wit Trans. Built Environ.* **2020**, *198*, 29–39.
112. Pannell, J.; Panoutsos, G.; Cooke, S.; Pope, D.; Rigby, S. Predicting specific impulse distributions for spherical explosives in the extreme near-field using a Gaussian function. *Int. J. Prot. Struct.* **2021**, *12*, 437–459. [[CrossRef](#)]
113. Becker, M.; Klavzar, A.; Wolf, T.; Renck, M. Data-driven prediction of plate velocities and plate deformation of explosive reactive armor. *Def. Technol.* **2022**, *18*, 2141–2149. [[CrossRef](#)]
114. Bortolan Neto, L.; Saleh, M.; Pickerd, V.; Yiannakopoulos, G.; Mathys, Z.; Reid, W. Rapid mechanical evaluation of quadrangular steel plates subjected to localised blast loadings. *Int. J. Impact Eng.* **2020**, *137*, 103461. [[CrossRef](#)]
115. Pannell, J.; Rigby, S.; Panoutsos, G. Physics-informed regularisation procedure in neural networks: An application in blast protection engineering. *Int. J. Prot. Struct.* **2022**, *13*, 555–578. [[CrossRef](#)]
116. Pannell, J.; Rigby, S.; Panoutsos, G. Application of transfer learning for the prediction of blast impulse. *Int. J. Prot. Struct.* **2022**, *ahead of print*.
117. Flood, I.; Bewick, B.; Rauch, E. Rapid Simulation of Blast Wave Propagation in Built Environments Using Coarse-Grain Simulation. *Int. J. Prot. Struct.* **2012**, *3*, 431–448. [[CrossRef](#)]
118. Kang, M.A.; Park, C.H. Prediction of Peak Pressure by Blast Wave Propagation Between Buildings Using a Conditional 3D Convolutional Neural Network. *IEEE Access* **2023**, *11*, 26114–26124. [[CrossRef](#)]
119. Zahedi, M.; Golchin, S. Prediction of blast loading on protruded structures using machine learning methods. *Int. J. Prot. Struct.* **2023**, *ahead of print*.
120. Winter, K.O.; Hargather, M.J. Three-dimensional shock wave reconstruction using multiple high-speed digital cameras and background-oriented schlieren imaging. *Exp. Fluids* **2019**, *60*, 1–13. [[CrossRef](#)]
121. Settles, G.S.; Hargather, M.J. A review of recent developments in schlieren and shadowgraph techniques. *Meas. Sci. Technol.* **2017**, *28*, 042001. [[CrossRef](#)]
122. Hargather, M.J.; Settles, G.S. Natural-background-oriented schlieren imaging. *Exp. Fluids* **2010**, *48*, 59–68. [[CrossRef](#)]

123. Mizukaki, T.; Tsukada, H.; Wakabayashi, K.; Matsumura, T.; Nakayama, Y. Quantitative visualization of open-air explosions by using background-oriented schlieren with natural background. In Proceedings of the 28th International Symposium on Shock Waves, Manchester, UK, 17–22 July 2012; Springer: Berlin/Heidelberg, Germany, pp. 465–470.
124. Higham, J.E.; Isaac, O.S.; Rigby, S.E. Optical flow tracking velocimetry of near-field explosions. *Meas. Sci. Technol.* **2022**, *33*, 047001. [[CrossRef](#)]
125. Dela Cueva, J.C.A.; Zheng, L.; Lawlor, B.; Nguyen, K.T.; Westra, A.; Nunez, J.; Zanteson, J.; McGuire, C.; Chavez Morales, R.; Katko, B.J.; et al. Blast wave interaction with structures: An application of exploding wire experiments. *Multiscale Multidiscip. Model. Exp. Des.* **2020**, *3*, 337–347. [[CrossRef](#)]
126. Zheng, L.; Lawlor, B.; Katko, B.; McGuire, C.; Zanteson, J.; Eliasson, V. Image processing and edge detection techniques to quantify shock wave dynamics experiments. *Exp. Tech.* **2021**, *45*, 483–495. [[CrossRef](#)]
127. Hargather, M.J.; Settles, G.S. Retroreflective shadowgraph technique for large-scale flow visualization. *Appl. Opt.* **2009**, *48*, 4449–4457. [[CrossRef](#)] [[PubMed](#)]
128. Edgerton, H.E. Shock wave photography of large subjects in daylight. *Rev. Sci. Instruments* **1958**, *29*, 171–172. [[CrossRef](#)]
129. Edgerton, H.E. *Electronic Flash, Strobe*; McGraw-Hill: New York, NY, USA, 1970.
130. Slangen, P.; Lauret, P.; Aprin, L.; Heymes, F.; Lecysyn, N. Optical characterizations of falling droplets interacting with shock wave. In Proceedings of the 10th Pacific Symposium on Flow Visualization and Image Processing (PSFVIP10), Naples, Italy, 15–18 June 2015.
131. Watson, S.; MacPherson, W.; Barton, J.; Jones, J.; Tyas, A.; Pichugin, A.; Hindle, A.; Parkes, W.; Dunare, C.; Stevenson, T. Investigation of shock waves in explosive blasts using fibre optic pressure sensors. *Meas. Sci. Technol.* **2006**, *17*, 1337. [[CrossRef](#)]
132. Schenato, L. A review of distributed fibre optic sensors for geo-hydrological applications. *Appl. Sci.* **2017**, *7*, 896. [[CrossRef](#)]
133. Cheval, K.; Loiseau, O.; Vala, V. Laboratory scale tests for the assessment of solid explosive blast effects. Part I: Reflected blast series of tests. *J. Loss Prev. Process Ind.* **2010**, *23*, 613–621. [[CrossRef](#)]
134. Cheval, K.; Loiseau, O.; Vala, V. Laboratory scale tests for the assessment of solid explosive blast effects. Part II: Reflected blast series of tests. *J. Loss Prev. Process Ind.* **2012**, *25*, 436–442. [[CrossRef](#)]
135. Rigby, S.E.; Fay, S.D.; Tyas, A.; Warren, J.A.; Clarke, S.D. Angle of incidence effects on far-field positive and negative phase blast parameters. *Int. J. Prot. Struct.* **2015**, *6*, 23–42. [[CrossRef](#)]
136. Quinn, M.K.; Kontis, K. Pressure-Sensitive Paint Measurements of Transient Shock Phenomena. *Sensors* **2013**, *13*, 4404–4427. [[CrossRef](#)] [[PubMed](#)]
137. Quinn, M.K.; Stokes, N.; Roberts, D.; Lang, J. Use of Pressure Sensitive Paint as a Blast Diagnostic. *Explos. Eng.* **2023**, 31–33.
138. Hegde, G.; Prasad, M.; Asokan, S. Temperature compensated diaphragm based Fiber Bragg Grating (FBG) sensor for high pressure measurement for space applications. *Microelectron. Eng.* **2021**, *248*, 111615. [[CrossRef](#)]
139. Ma, W.; Jiang, Y.; Hu, J.; Jiang, L.; Zhang, T. Microelectromechanical system-based, high-finesse, optical fiber Fabry–Perot interferometric pressure sensors. *Sensors Actuators Phys.* **2020**, *302*, 111795. [[CrossRef](#)]
140. Clarke, S.; Fay, S.; Warren, J.; Tyas, A.; Rigby, S.; Elgy, I. A large scale experimental approach to the measurement of spatially and temporally localised loading from the detonation of shallow-buried explosives. *Meas. Sci. Technol.* **2014**, *26*, 015001. [[CrossRef](#)]
141. Rigby, S.; Fay, S.; Clarke, S.; Tyas, A.; Reay, J.; Warren, J.; Gant, M.; Elgy, I. Measuring spatial pressure distribution from explosives buried in dry Leighton Buzzard sand. *Int. J. Impact Eng.* **2016**, *96*, 89–104. [[CrossRef](#)]
142. Rigby, S.; Fay, S.; Tyas, A.; Clarke, S.; Reay, J.; Warren, J.; Gant, M.; Elgy, I. Influence of particle size distribution on the blast pressure profile from explosives buried in saturated soils. *Shock Waves* **2018**, *28*, 613–626. [[CrossRef](#)]
143. Clarke, S.; Rigby, S.; Fay, S.; Barr, A.; Tyas, A.; Gant, M.; Elgy, I. Characterisation of buried blast loading. *Proc. R. Soc. Math. Phys. Eng. Sci.* **2020**, *476*, 20190791. [[CrossRef](#)] [[PubMed](#)]
144. Rigby, S.E.; Tyas, A.; Clarke, S.D.; Fay, S.D.; Reay, J.J.; Warren, J.A.; Gant, M.; Elgy, I. Observations from Preliminary Experiments on Spatial and Temporal Pressure Measurements from Near-Field Free Air Explosions. *Int. J. Prot. Struct.* **2015**, *6*, 175–190. [[CrossRef](#)]
145. Hopkinson, B. A method of measuring the pressure produced in the detonation of high explosives or by the impact of bullets. *Philos. Trans. R. Soc. Lond.* **1914**, *213*, 437–456.
146. Edwards, D.H.; Thomas, G.O.; Milne, A.; Hooper, G.; Tasker, D. Blast wave measurements close to explosive charges. *Shock Waves* **1992**, *2*, 237–243. [[CrossRef](#)]
147. Puckett, A.; Peterson, M. Individual longitudinal Pochhammer-Chree modes in observed experimental signals. *Acoust. Res. Lett. Online* **2005**, *6*, 268–273. [[CrossRef](#)]
148. Puckett, A.; Peterson, M. A semi-analytical model for predicting multiple propagating axially symmetric modes in cylindrical waveguides. *Ultrasonics* **2005**, *43*, 197–207. [[CrossRef](#)] [[PubMed](#)]
149. Taylor, L.C.; Fourney, W.L.; Leiste, H.U. Pressures on Targets From Buried Explosions. *Int. J. Blasting Fragm.* **2010**, *4*, 165–192.
150. Tyas, A.; Ozdemir, Z. On backward dispersion correction of Hopkinson Pressure Bar signals. *Philos. Trans. R. Soc. Lond. Ser. Math. Phys. Eng. Sci.* **2014**, *372*, 20130291. [[CrossRef](#)] [[PubMed](#)]
151. Cloete, T.; Nurick, G. Blast characterization using a ballistic pendulum with a centrally mounted Hopkinson bar. *Int. J. Prot. Struct.* **2016**, *7*, 367–388. [[CrossRef](#)]
152. Cui, X.; Yao, X.; Chen, Y. A lab-scale experiment approach to the measurement of wall pressure from near-field under water explosions by a Hopkinson bar. *Shock Vib.* **2018**, *8273469*, 1–15. [[CrossRef](#)]

153. Yao, X.; Cui, X. Guo, K.; Chen, Y. An experimental approach to the measurement of wall pressure generated by an underwater spark-generated bubble by a Hopkinson bar. *Shock Vib.* **2019**, *2019*, 5341317.
154. Barr, A.; Rigby, S.; Clayton, M. Correction of higher mode Pochhammer–Chree dispersion in experimental blast loading measurements. *Int. J. Impact Eng.* **2020**, *139*, 103526. [[CrossRef](#)]
155. Barr, A.D.; Rigby, S.E.; Clarke, S.D.; Farrimond, D.; Tyas, A. Temporally and Spatially Resolved Reflected Overpressure Measurements in the Extreme Near Field. *Sensors* **2023**, *23*, 964. [[CrossRef](#)] [[PubMed](#)]
156. Rigby, S.E.; Barr, A.D.; Clayton, M. A review of Pochhammer–Chree dispersion in the Hopkinson bar. *Proc. Inst. Civ. Eng. Eng. Comput. Mech.* **2018**, *171*, 3–13. [[CrossRef](#)]
157. Blanc, L.; Hanus, J.L.; William-Louis, M.; Le-Roux, B. Experimental and Numerical Investigations of the Characterisation of Reflected Overpressures around a Complex Structure. *J. Appl. Fluid Mech.* **2016**, 121–129.
158. Courtiaud, S.; Lecysyn, N.; Damamme, G.; Poinot, T.; Selle, L. Analysis of mixing in high-explosive fireballs using small-scale pressurised spheres. *Shock Waves* **2019**, *29*, 339–353. [[CrossRef](#)]
159. Tamba, T.; Sugiyama, Y.; Wakabayashi, K.; Matsumura, T.; Nakayama, Y. Additional protection to a standard wall against blast wave—Effect of the shape and position of the additional wall. *Sci. Technol. Energetic Mater.* **2021**, *82*, 75–82.
160. Bae, J.; Byun, H.; Yoon, T.; Carter, C.D.; Do, H. Novel calibration-free seedless velocimetry using laser-induced shockwave. *Exp. Therm. Fluid Sci.* **2021**, *126*, 110384. [[CrossRef](#)]
161. Valentino, T. Analytical model to determine the relevant parameters governing the transferred momentum to spherical indenters by laser-induced shock waves. *Opt. Lasers Eng.* **2021**, *145*, 106670. [[CrossRef](#)]
162. Kimblin, C.; Trainham, R.; Capelle, G.A.; Mao, X.; Russo, R.E. Characterization of laser-induced plasmas as a complement to high-explosive large-scale detonations. *AIP Adv.* **2017**, *7*, 095208. [[CrossRef](#)]
163. Isaac Samuelraj, O.; Jagadeesh, G.; Kontis, K. Micro-blast waves using detonation transmission tubing. *Shock Waves* **2013**, *23*, 307–316. [[CrossRef](#)]
164. Gajewski, T.; Sielicki, P.W. Experimental study of blast loading behind a building corner. *Shock Waves* **2020**, *30*, 385–394. [[CrossRef](#)]
165. Denny, J.; Langdon, G.; Rigby, S.; Dickinson, A.; Batchelor, J. A numerical investigation of blast-structure interaction effects on primary blast injury risk and the suitability of existing injury prediction methods. *Int. J. Prot. Struct.* **2022**, *ahead of print*.
166. Fischer, K.; Häring, I.; Riedel, W.; Vogelbacher, G.; Hiermaier, S. Susceptibility, vulnerability, and averaged risk analysis for resilience enhancement of urban areas. *Int. J. Prot. Struct.* **2016**, *7*, 45–76. [[CrossRef](#)]
167. Vogelbacher, G.; Häring, I.; Fischer, K.; Riedel, W. Empirical Susceptibility, Vulnerability and Risk Analysis for Resilience Enhancement of Urban Areas to Terrorist Events. *Eur. J. Secur. Res.* **2016**, *1*, 151–186. [[CrossRef](#)]
168. Dennis, A.A.; Smyl, D.J.; Stirling, C.G.; Rigby, S.E. A branching algorithm to reduce computational time of batch models: Application for blast analyses. *Int. J. Prot. Struct.* **2022**, *ahead of print*.

**Disclaimer/Publisher’s Note:** The statements, opinions and data contained in all publications are solely those of the individual author(s) and contributor(s) and not of MDPI and/or the editor(s). MDPI and/or the editor(s) disclaim responsibility for any injury to people or property resulting from any ideas, methods, instructions or products referred to in the content.